Simon Halbritter, BSc

# Surface Dynamics and Phonon Dispersion of $Sb_2Te_3(111)$ from Helium Atom Scattering

**MASTER'S THESIS**

to achieve the university degree of

Diplom-Ingenieur

Master's degree programme: Technical Physics

submitted to

**Graz University of Technology**

Supervisor

Univ.-Prof. Dipl-Phys. Dr.rer.nat. Wolfgang E. Ernst

Institute of Experimental Physics

Co-Supervisor

Dr. Anton Tamtögl

Graz, March, 2020

## AFFIDAVIT

I declare that I have authored this thesis independently, that I have not used other than the declared sources/resources, and that I have explicitly indicated all material which has been quoted either literally or by content from the sources used. The text document uploaded to TUGRAZonline is identical to the present master‘s thesis.

Date

Signature

# Abstract

In this work the surface dynamical properties of the three-dimensional topolocial insulator (TI) $Sb_2Te_3(111)$ were investigated experimentally, using helium atom scattering. TIs are a new type of quantum material, insulating in the bulk, but with metallic states at the surface. This rather new class of materials has attracted great interest recently, due to possible applications in non-linear optics, thermoelectric and spin transport electronic devices. Compared to other binary TIs such as $Bi_2Se_3$ and $Bi_2Te_3$, $Sb_2Te_3$ is much less studied. In particular information about the surface dynamical properties are scarce and the surface phonon dispersion has not been studied experimentally up to now. $Sb_2Te_3$ is known as a naturally p-doped semiconductor with prominent thermoelectric properties, especially at room temperature. Moreover, in contrast to other binary TIs, $Sb_2Te_3$ exhibits a Fermi level above the Dirac point.
Helium atom scattering (HAS) is the most appropriate technique for obtaining relevant experimental information of dynamical processes from surfaces, since the scattering particle strictly interacts with the electron cloud of surface atoms and allows for a non destructive surface investigation.
From the obtained diffraction pattern, the surface lattice constant was determined with $a = (4.242 \pm 0.006)\,\text{Å}$ at room temperature and $a = (4.225 \pm 0.006)\,\text{Å}$ at a sample temperature of -160 °C, corresponding to a linear thermal expansion of $\alpha = (2.2 \pm 0.8) \cdot 10^{-5}\ \text{K}^{-1}$. By applying the Debye-Waller model to the measurements of the thermal attenuation of elastic scattering intensities, a surface Debye-temperature of $\theta_D = (141 \pm 3)\,\text{K}$ was obtained. With a recently introduced method, the mass enhancement factor for electron-phonon coupling at the surface can be determined, based on the Debye-Waller measurement, with $\lambda = 0.14$.
Inelastic scattering events were observed via time of flight (TOF) measurements. Over 300 TOF measurements were carried out along the two high symmetry directions, for various incident energies and incident angles. The TOF spectra were transferred to energy scale, allowing to identify phonon creation and annihilation events. The obtained phonon energies and their corresponding wave vector, based on the conservation of momentum and energy, allow to measure the surface phonon dispersion over the entire Brillouin zone. The surface phonon dispersion was compared with theoretical calculations from density functional perturbation theory with reasonably good agreement. From the slope of the Rayleigh mode the speed of sound was determined as $1794\,\text{m}\,\text{s}^{-1}$. Beside the expected surface phonon modes, several low energy events were observed below the Rayleigh wave, possibly coming from collective electronic excitations.

# Kurzfassung

Im Rahmen der vorliegenden Masterarbeit wurde die Oberfläche des dreidimensionalen topologischen Isolators (TI) $Sb_2Te_3(111)$ mittels Heliumstreung untersucht.
Der Begriff TI beschreibt einen Festkörper, welcher in seinem Inneren elektrisch nichtleitend ist, jedoch an der Oberfläche lokaliserte, leitende Zustände besitzt, welche die Bandlücke schließen. TIs besitzen potentielle Einsatzmöglichkeiten in nichtlinerarer Optik, thermoelektrischen und spinelektronischen Anwendungen.
Aufgrund der hervorragenden thermoelektrischen Eigenschaften, speziell bei Raumtemperatur, findet $Sb_2Te_3$ vielfach Einsatz in Thermoelementen, elektrischen Wärmepumpen und thermoelektrischen Generatoren. Im Gegensatz zu strukturell vergleichbaren TIs wie $Bi_2Se_3$ und $Bi_2Te_2Se$, liegt der Dirac-Punkt der leitenden Zustände des von Natur aus p-dotierten Halbleiters $Sb_2Te_3$ über dessen Ferminiveau. $Sb_2Te_3$ wurde bisher noch kaum untersucht. Speziell zur Oberflächendynamik dieses Materials exisiteren zu diesem Zeitpunkt nur wenig experimentelle Daten.
Heliumstreuung ist für die Untersuchung von Vibrationszuständen an der Oberfläche bestens geeignet. Der niederenergetische Heliumstrahl wechselwirkt ausschließlich mit der Ladungsverteilung der Oberflächenatome, was eine zerstörungsfreie und oberflächensensitive Untersuchung ermöglicht.
Über die bei elastischer Streuung auftretenden Beugungsmuster wurde die Gitterkonstante an der Oberfläche zu $a = (4.242 \pm 0.006)\,\text{Å}$ bei Raumtemperatur, sowie $a = (4.225 \pm 0.006)\,\text{Å}$ bei einer Probentemperatur von $-160\,°\text{C}$ ermittelt. Daraus wurde ein linearer, thermischer Ausdehnungskoeffizient von $\alpha = (2.2 \pm 0.8) \cdot 10^{-5}\,\text{K}^{-1}$ bestimmt. Mithilfe der Debye-Waller Näherung, wurde aus der thermischen Abnahme elastischer Streuprozzese, die Oberflächen Debyetemperatur mit $\theta_D = (141 \pm 3)\,\text{K}$ ermittelt. Die Elektron-Phonon Kopplungskonstante $\lambda = 0.14$ wurde basierend auf einer Analyse der Debye-Waller Messungen, durch die Anwendung einer vor kurzem neu eingeführten Methode bestimmt.
Das Hauptaugenmerk dieser Arbeit lag auf der Untersuchung inelastischer Streuprozesse welche am experimentellen Aufbau mittels Flugzeitmessungen durchgeführt wurden. Die Auswertung von über 300 Messungen entlang der beiden Symmetrierichtungen, für unterschiedliche Einfallswinkel und Energien führte zu der Oberflächenphonondispersion für die komplette Brillouin-Zone. Diese zeigt gute Übereinstimmung im Vergleich zu theoretischen Berechnungen auf Basis

der störungstheoretischen Dichtefunktionaltheorie. Aus der linearen Steigung der Rayleighwelle wurde die Schallgeschwindigkeit mit $1794\,\mathrm{m\,s^{-1}}$ bestimmt.
Neben den zu erwartenden Phononenmoden, wurden weitere inelastische Streuprozesse im Energiebereich unterhalb der Rayleighwelle beobachtet, welche keiner Oberflächenphononenmode zugeordnet werden können. Diese niederenergetischen Ereignisse sind möglicherweise auf kollektive Elektronenanregungen zurückzuführen.

# Contents

# 1 Introduction

Antimony telluride ($Sb_2Te_3$) is a material, which serves in many applications, due to its various functional properties. It is used as phase-change material in optical data storage [1] and is among the most important thermoelectric materials at room temperature [2].
$Sb_2Te_3$ belongs to a class of condensed matter materials called three-dimensional topological insulators (TI) [3]. TIs are described as a new type of quantum material, where the band gap present in the bulk, is closed by topologically protected surface states, forming a single Dirac-cone at the $\overline{\Gamma}$-point.
In contrast to similar binary TIs, such as $Bi_2Se_3$ and $Bi_2Te_3$, the Fermi-level of intrinsically p-doped $Sb_2Te_3$ is located below the Dirac-point [4]. In addition, $Sb_2Te_3$ can exhibit hole pockets in the $\overline{\Gamma M}$ direction, depending on the position of the Fermi-level.
While the surface electronic states of $Sb_2Te_3(111)$ have been investigated, by angle resolved photoemission spectroscopy [5–7] and theoretical band structure calculations [8], only few experimental data exists for the surface dynamical properties.

Within the course of this work, helium atom scattering (HAS) was used for an experimental study of the surface vibrational modes of $Sb_2Te_3(111)$. HAS is very well suited to deliver information of surface dynamics, since the low energetic helium atoms strictly interact with the electron density of the surface atoms, allowing a non-destructive and surface sensitive analysis of the material.
Elastic scattering processes are used to determine crystal properties such as the surface lattice constant and the thermal expansion. Measurements of the thermal attenuation further provide information about the surface Debye-temperature and the electron-phonon interaction.
Inelastic scattering events are observed in terms of time of flight measurements and used to determine the surface phonon dispersion, which is compared with *ab−initio* calculations. In addition, the speed of sound on the surface is determined from the TOF data close to the $\overline{\Gamma}$-point.

# 2 Experimental Setup

This chapter will give a quick overview of the experimental setup. A more detailed description can be found in the PhD thesis of Anton Tamtögl [9].
The apparatus, on which the measurements of this thesis were carried out, was originally constructed at the FU Berlin and transferred to the TU Graz in the year 2007 [10] and later adapted and characterized [9].
The main purpose of the aparaturs, called H.A.N.S. (for Helium Atom Non-destructive Scattering), is to provide a quasi monochromatic helium beam for elastic and inelastic scattering experiments on surfaces of various crystalline materials and adsorbates as well as the detection of angle resolved scattering intensity for analysis, to obtain information of the surface structure and properties. It consists of a helium source, the main chamber, which contains the sample mounting and a detection arm with a quadrupole massspectrometer. The whole apparatus is illustrated in figure 2.1.
To run scattering experiments, high vacuum for the beam generation and detection is necessary. The main chamber is kept under ultra high vacuum conditions to keep the sample clean from adsorbates. The apparatus exhibits several chambers with different pressure ranges and various vacuum pumps, represented by the red parts. Additionally a load lock chamber was attached [11, 12] to the main chamber for a more convenient sample exchange.

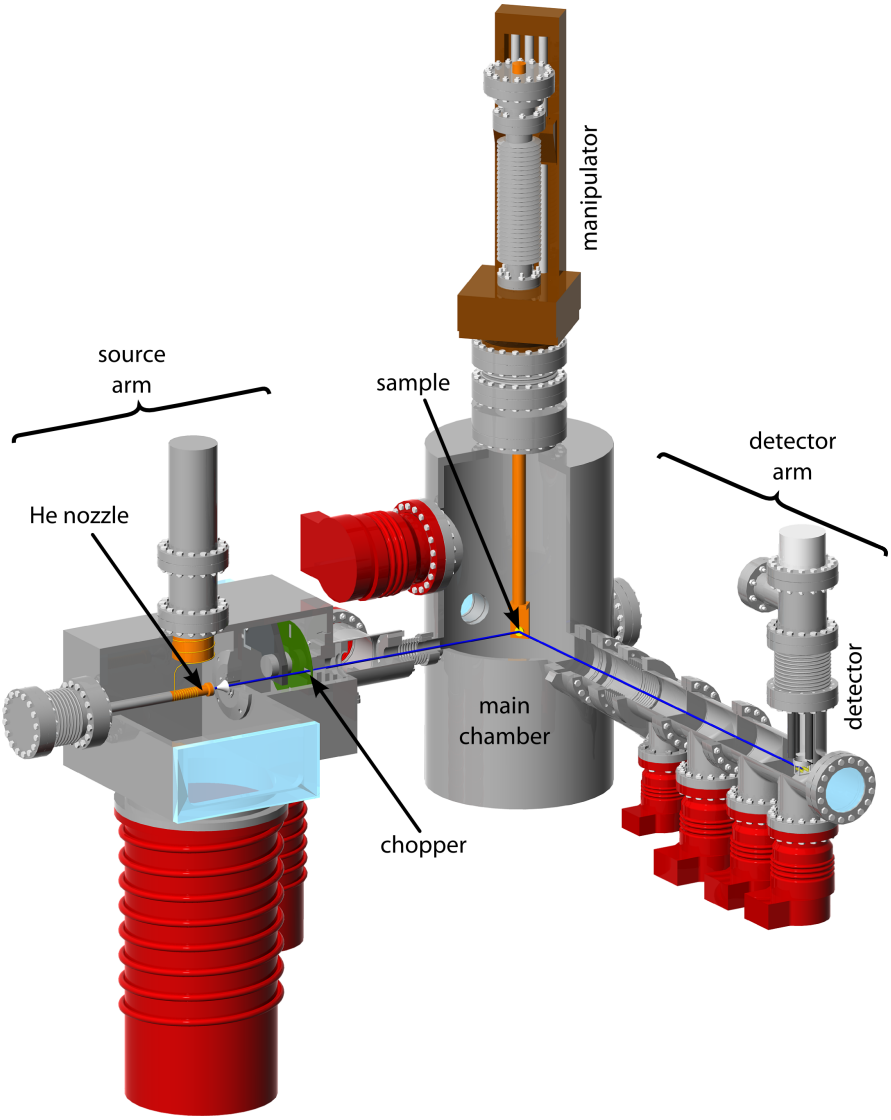


Figure 2.1: CAD illustration of the apparatus used for the measurements, taken from A.Tamtögl [9]. The He beam (blue) generated in the source arm, interacts with the sample in the main chamber. Scattered He atoms are observed by a quadrupole mass spectrometer in the detector arm.

## 2.1 Source Arm

The source arm (figure 2.1) provides the helium beam used for the scattering experiments. It consists of two separated chambers (see figure 2.2) which contain the helium source and the mounting of the chopper (section 2.1.2). The chopper is needed for time of flight measurements and can be shifted into the beam, to cut it into small packets.

### 2.1.1 Beam Generation

For scattering experiments it is crucial to provide a beam of helium particles, which is well collimated and shows a very narrow spread in velocity to achieve high resolution in diffraction experiments and also be able to resolve small velocity differences in time of flight measurements.
To accomplish this, helium gas is led from a supply with a high pressure of $p_0 \sim 50\,\text{bar}$ through a cooled (45 K - 170 K), narrow nozzle of 10 µm diameter.
The gas spreads out quickly by a supersonic expansion, where the mean free path of the atoms is small compared to the nozzle diameter, into the low pressure region ($p_a < 10^{-6}\,\text{mbar}$) of the first vacuum chamber of the source-arm. After leaving the nozzle, the helium beam changes from a continuous flow to a molecular flow. A skimmer, placed beyond the continuous region, separates the middle part of the helium beam and transfers into the second vacuum chamber, where the helium beam passes finally through an aperture into the main chamber. The passage to the main chamber can be closed by a valve to help keep the vacuum in the main chamber in the UHV range, when no measurements are carried out.
Since the above described expansion happens very fast it can be assumed as adiabatic. The thermal energy of the helium particle thereby is transformed into translational kinetic energy, which converts a Maxwell-Boltzmann velocity distribution to a very defined peak (see also 2.3).
In good approximation helium can be treated as an ideal gas. Therefore the expansion is described in terms of thermodynamics and conservation of energy to derive the final particle velocity [13, 14], with the Boltzmann constant $k_B$, the helium mass $m_{He}$ and the temperature of the nozzle $T_0$.

$$v \approx \sqrt{\frac{5 \cdot k_B \cdot T_0}{m_{He}}} \tag{2.1}$$

From the velocity the incident Energy $E_i$ and further the particle wave vector $|\mathbf{k_i}|$ can be derived.

$$E_i = \frac{5}{2} \cdot k_B \cdot T_0 \tag{2.2}$$

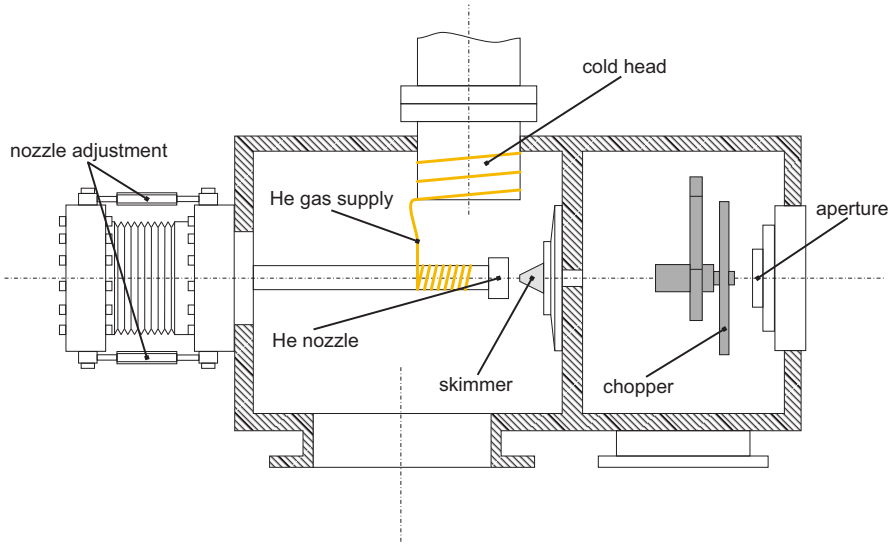


Figure 2.2: Schematic sketch of the Helium source after the CAD template from [9].

$$|\mathbf{k_i}| = \sqrt{\frac{2 \cdot m_{He}}{\hbar^2} \cdot E_i} \tag{2.3}$$

The temperature of the nozzle $T_0$ is controlled by a cold head (Gifford-McMahon cooler), a resistive heater and measured with a Pt100 temperature sensor. By varying the nozzle temperature $T_0$, the velocity of the particles and therefore the incident energy $E_i$ and the wave vector $\mathbf{k_i}$ of the Helium beam can be adjusted to the requirements of the experiment.

### 2.1.2 Chopper

For time of flight measurements it is important to distinguish between particle packets. This allows for the determination of a flight time and further a velocity and energy to those. This obviously can not be done with a continuous atom beam. An easy way to split up the beam in several packets, is to install a so called chopper disk. In the simplest form the chopper disk consists of a rotating plate with a small slit. The plate blocks of the atom beam, letting only a small fraction of the beam pass through the slit, once per rotation.
The disks rotation frequency and therefore its position at a specific time are determined by an optical barrier and an additional slit on the disk. In the apparatus used for measurements in this work, to achieve a better beam intensity, a pseudo random chopper disk was used (section 3.9.2).
The signal analysis, including the deconvolution and transformation to an energy spectrum are discussed in section 3.9.

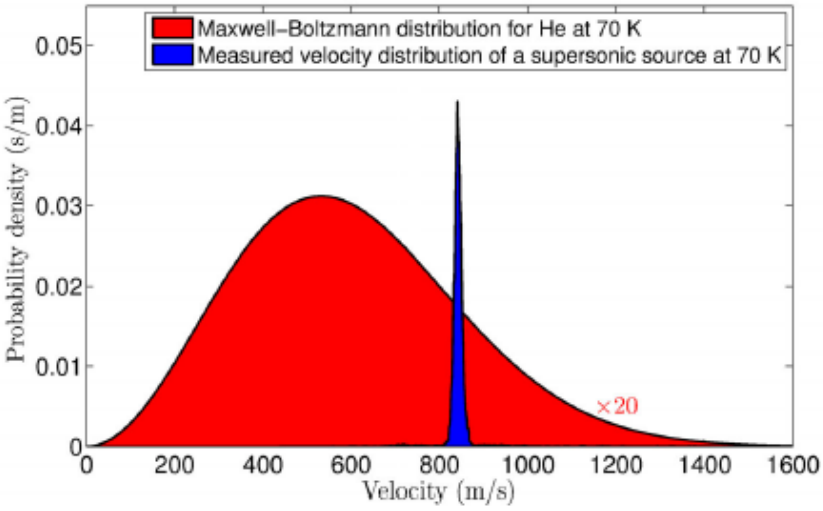


Figure 2.3: Comparison of the velocity distribution of the helium gas at the source and after the supersonic expansion [9].

## 2.2 Main Chamber

In the main chamber the scattering events take place. It is kept in ultra high vacuum range ($p = 10^{-10} - 10^{-11}$ mbar) by turbo molecular pumps to guarantee long mean free path lengths of the helium particle and to keep the sample surface clean from adsorbats as long as possible. To measure the composition of the residual gas, the main chamber is equipped with a quadrupole mass spectrometer. The sample to be analysed, is mounted on a seven axis manipulator, which allows to rotate and move it in various directions, to adjust the sample to the requirements of a measurement. Further the manipulator features a liquid nitrogen reservoir. A thermal connection from the reservoir to the sample holder is provided by copper braids to vary the temperature of the sample. If required, the sample surface can be sputtered with an installed argon-ion gun and annealed by a button heater, mounted on the sample holder. For alignment of the crystalline sample in high symmetry directions, a LEED (low energy electron diffraction) is used, which in combination with an AES (Auger electron spectroscopy), also provides monitoring of the grade of contamination of the sample surface.

## 2.3 Detection Arm

The detector arm is connected to the main chamber in a fixed angle of $\theta_{SD}$= 91.5° [9] to the source arm entrance. It consists of several differentially pumped stages,

so background particles get pumped out and only directly scattered helium atoms arrive at the quadrupole mass spectrometer (QMS). The QMS signal is recorded by a multi-channel analyser for further evaluation.

# 3 Theoretical Background

## 3.1 Description of a Crystal Surfaces

In solid states physics an ideal crystal is created by the infinite repetition of a basis attached to a periodic lattice, called Bravais lattice, generated by discrete translations by integers $(j_1, j_2, j_3)$ and the basis vectors $(\mathbf{a}, \mathbf{b}, \mathbf{c})$, which span the unit cell [15].

$$\mathbf{r_j} = j_1\mathbf{a} + j_2\mathbf{b} + j_3\mathbf{c} \tag{3.1}$$

To get a periodic surface structure, one can imagine to cut through the bulk of an ideal crystal along a specific plane. Derived from the description of the crystal structure in bulk materials, the surface of such a crystal can also be described by the two integers $j_1, j_2$ and the translation vectors $\mathbf{a}$ and $\mathbf{b}$, which span the surface unit cell.

$$\mathbf{R_j} = j_1\mathbf{a} + j_2\mathbf{b} \tag{3.2}$$

## 3.2 Reciprocal Lattice for Two Dimensions

The concept of a reciprocal lattice is very important in all sorts of structure analysis concerning diffraction experiments and can be used in the same way for surfaces.
To every Bravais lattice, as discussed in section 3.1, a corresponding reciprocal lattice can be assigned, described by the two dimensional reciprocal primitive vectors, calculated from primitive vectors in real space (see equation 3.3).

$$\mathbf{a}^* = 2\pi\frac{\mathbf{a}\times\mathbf{n}}{\mathbf{a}\cdot(\mathbf{b}\times\mathbf{n})} \qquad \mathbf{b}^* = 2\pi\frac{\mathbf{n}\times\mathbf{a}}{\mathbf{a}\cdot(\mathbf{b}\times\mathbf{n})} \tag{3.3}$$

$\mathbf{n}$ is the normalised surface vector perpendicular to the plane spanned by $\mathbf{a}$ and $\mathbf{b}$ and replaces the basis vector $\mathbf{c}$ from the three dimensional description. The coordinates of the reciprocal lattice points can be reached by translation of the reciprocal basis vector with the integers $h$ and $k$, also known as the Miller indices,

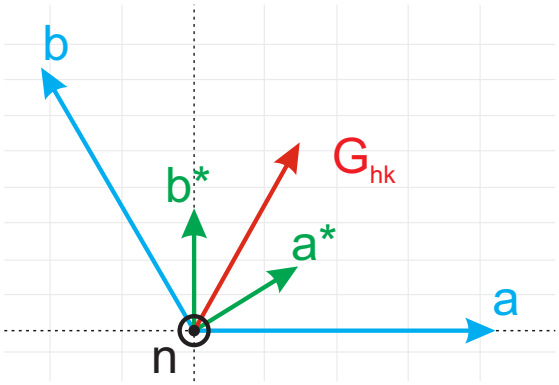


Figure 3.1: Sketch of the basis vectors in real space and their reciprocal lattice vectors.

yielding the reciprocal lattice vector $\mathbf{G}_{hk}$.

$$\mathbf{G}_{hk} = h\mathbf{a}^* + k\mathbf{b}^* \tag{3.4}$$

Analog to the Wigner-Seitz cell in real-space, a primitive unit cell can be constructed from the reciprocal lattice, called first Brillouin zone [15].

## 3.3 Helium Atom Scattering

Helium atom scattering (HAS) is a proper technique for analysing surface structures and besides electron energy loss spectroscopy (EELS), the preferred method to study surface dynamics of crystalline and amorphous surfaces [16].
In comparison to other scattering techniques like X-ray diffraction, electron or neutron scattering, which typically get scattered at the nuclei of an atom, incoming helium particles interact only with the electron density cloud of the outer-most layer of atoms. The interaction can be described by a surface potential, which is founded in strong Pauli repulsion and a weak van der Waals attraction. The atom surface leads to a periodic corrugated potential.
Since helium is electrically, magnetically and chemically inert and the incident energies are in a range of only 10 to 200 meV, helium atom scattering leads to a completely non-destructive investigation of a sample surface and even weakly bound adsorbats [17]. HAS is very well suited for structure analysis of semiconductors and insulators, where the electrons are close to the ion cores. This means, that the scattered helium atoms strictly only probe the surface of a material.
Another big advantage comes from the high scattering cross section of helium atoms of about 100 Å, which make them very sensible for defects and impurities at the surface. Since these break the periodicity, helium atoms will scatter diffusely and will not contribute to the diffraction pattern. As figure 3.2 suggests,

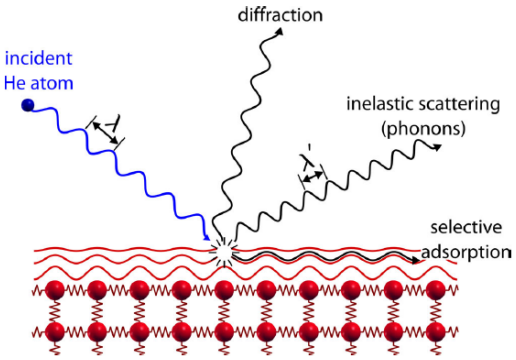


Figure 3.2: This figure simplified shows the various scattering processes, which can occur in HAS [9].

during HAS several scattering processes can occur. The particle energy ($E_i = E_f$) does not change for elastic scattering processes (diffraction).
For inelastic scattering processes, energy is transferred from or to the sample ($\Delta E = E_f - E_i$). Finally, selective adsorption can occur, if the incident energy is in the range of the attractive potential of the surface.

## 3.4 Diffraction from Periodic Structures

A monochromatic helium beam can also be described as a travelling wave with an ascribed de Broglie wavelength $\lambda_i$.

$$\lambda_i = \frac{h}{m_{He} \cdot v} = \frac{h}{p} \tag{3.5}$$

For a diffraction pattern to arise upon scattering from a periodic surface, the wavelength has to be of the same order of magnitude, as the lattice periodicity of the surface-structure. The scattered intensity then shows various peaks due to constructive interference, depending on the incident angle. The angles for constructive interference are described by the Laue-Condition (3.6).

$$\Delta K = \mathbf{K}_i - \mathbf{K}_f = \mathbf{G}_{hk} \tag{3.6}$$

$$E_i = E_f \tag{3.7}$$

The surface-parallel parts of the incoming and outgoing wave vectors $\mathbf{K}_i$ and $\mathbf{K}_j$ only differ by a reciprocal lattice vector $\mathbf{G}_{hk}$, while the total energy of the scattered particle stays the same.

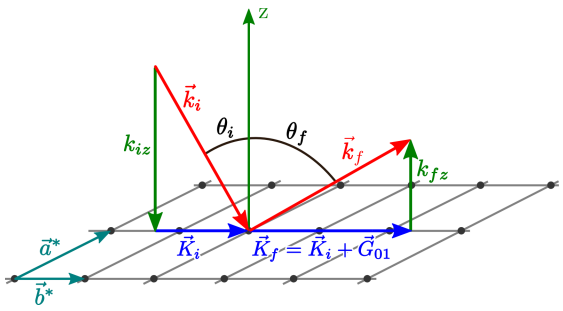


Figure 3.3: In this figure the geometry for elastic scattering is drawn. For $\mathbf{K}_f = \mathbf{K}_i + \mathbf{G}_{01}$ ($\mathbf{G}_{01} = \mathbf{G}_{hk}$) the *Laue Condition* is fulfilled [9].

## 3.5 Analysis of Surface Structure from Elastic Scattering

As already mentioned in chapter 2, the angle between the source-arm and the detector-arm $\theta_{SD}$ is fixed in the apparatus. This circumstance limits the measurable diffraction peaks from elastic scattering and also enters the scan curve equation, discussed in section 3.9.4.
Due to the geometry, the scattering process can only be measured in a plane perpendicular to the surface (see figure 3.3) and parallel to the incident and final wave vector $\mathbf{k}_i$ and $\mathbf{k}_f$. Their assigned parallel projections on the surface $\mathbf{K}_i, \mathbf{K}_f$ can be expressed as seen in equation 3.8:

$$\begin{aligned} |\mathbf{K}_i| &= |\mathbf{k}_i| \cdot \sin\theta_i \qquad \theta_i \ldots \text{ incident angle} \\ |\mathbf{K}_f| &= |\mathbf{k}_f| \cdot \sin\theta_f \qquad \theta_f \ldots\ldots \text{ final angle} \end{aligned} \tag{3.8}$$

For an elastic scattering event, the energy of the impinging particle is conserved, which also means, that the absolute values of the incoming and outgoing wave vectors are equal $|\mathbf{k}_i| = |\mathbf{k}_f|$.
Further due to the fixed angle, the sum of the incident and final angle has to be $\theta_{SD} = \theta_i + \theta_f$. Hence, in combination with the Laue Condition 3.6 and equations 3.8 an expression for the scattering condition for a specific incident angle can be derived 3.9.

$$\theta_i = \frac{\theta_{SD}}{2} - \arcsin\left[\frac{|\mathbf{G}_{hk}|}{2\,|\mathbf{k}_i|\cos\left(\frac{\theta_{SD}}{2}\right)}\right] \tag{3.9}$$

Using this expression, the reciprocal lattice vector $G_{hk}$ can be determined for a given incident angle $\theta_i$ and its wave vector $k_i(T_0)$. Further the expected position (incident angle) for diffraction peaks from constructive interference can be calculated for known structures.

## 3.6 Selective Adsorption

The interaction of closed shell helium atoms with the surface atoms of a probed sample can be described in terms of a short range repulsive and long range attractive surface potential [18]. This leads to a periodic corrugated potential wall, which the helium atom can penetrate to about 3 Angström above the top most ion core layer.
Selective Adsorption can occur, if the energy of the incident helium beam is of the same order of magnitude as the attractive potential well. The helium atom gets temporarily trapped in a bound state of the surface potential.
After a short time it is released again after interacting with a G-vector or a phonon. These so-called selective adsorption resonances can be seen in elastic scattering experiments and can be used to determine the surface potential of the probed material.

## 3.7 Debye-Waller Factor

The intensities from diffraction experiments also show a dependency of the sample temperature, which results from temperature induced inelastic scattering. The shape of the elastic diffraction peaks stays the same, but the overall intensity decreases due to the increasing contribution of inelastic scattering events.
This thermal attenuation can be taken in account by the Debye-Waller factor [18]:

$$I(T_S) = I_0 \cdot e^{-2W(T_S)}. \tag{3.10}$$

Equation 3.10 relates the intensity of elastic scattering events $I_0$ at temperature $T_0 = 0\,\mathrm{K}$, to the intensity depending on the sample temperature $I(T_S)$ with the Debye-Waller factor $W(T_S)$ in the exponent defined as:

$$2W(T_S) = \langle (\mathbf{u} \cdot \Delta\mathbf{k})^2_{T_S} \rangle \,. \tag{3.11}$$

The vector $\mathbf{u}$ describes the displacement of the lattice atoms from their equilibrium position and $\Delta\mathbf{k}$ the total change of momentum after the scattering event.
Since only specular contribution is observed, the momentum parallel to the surface can be neglected.

$$2W(T_S) = \langle u_z^2 \rangle \cdot (\Delta k_z)^2 \tag{3.12}$$

In first approximation the average squared atomic displacement $\langle u_z^2 \rangle$ perpendicular to the surface, can be treated as a harmonic oscillator

$$\langle u_z^2 \rangle = \frac{3k_B T}{M\omega^2}, \tag{3.13}$$

with $M$ being the effective mass of the surface atoms and $\omega$ the vibrational frequency, which is given by the Debye-frequency $\omega_D$.

$$\omega_D = \frac{k_B \theta_D}{\hbar} \tag{3.14}$$

The Debye-temperature $\theta_D$ is material specific and describes the occupied phonon states. In combination, all equations result in an expression for the Debye-Waller factor.

$$W(T_S) = \frac{3(\hbar^2 \Delta k_z^2) T_S}{2 M k_B \theta_D^2} \tag{3.15}$$

Until now, scattering processes were only determined by the plain structural properties of the surface. For a better approximation, also the attractive interaction in form of dispersion forces, needs to be taken into account. Incoming helium atoms are accelerated and decelerated when leaving the potential after scattering. This effect is described by the Beeby-correction [19]. The perpendicular momentum transfer $\Delta k_z$ is replaced by the expression 3.16 with an attractive potential with well depth $D$:

$$\Delta k_z = k_i \left[ \sqrt{\cos^2(\theta_f) + \frac{D}{E_i}} + \sqrt{\cos^2(\theta_i) + \frac{D}{E_i}} \right]. \tag{3.16}$$

Since, for the specular position $\theta_i = \theta_f$ and with the incident energy $E_i = \frac{\hbar^2 k_i^2}{2m}$, by applying the Beeby-correction, the Debye-Waller factor can be rewritten to:

$$W(T_S) = \frac{12 m [E_i \cos^2(\theta_i) + D] T_S}{M k_B \theta_D^2} \tag{3.17}$$

The temperature dependence of the Debye-Waller factor also determines the experimental condition for one-phonon experiments, since at higher temperatures, the contribution of multi-phonon processes becomes larger [18].

### 3.7.1 Electron-Phonon-Coupling

Recently a new quantum-theoretical derivation of elastic and inelastic scattering probabilities for He-atoms on metallic surfaces showed a direct proportionality of the Debye-Waller exponent with the electron-phonon coupling [20]. The Debye-Waller factor contains the sum over all contributing phonon modes and therefore can be used to determine the average electron-phonon coupling $\lambda_{HAS}$:

$$\lambda_{HAS} \cong \frac{1}{4\mathcal{N}(E_F)} \frac{m_e^*}{m} \frac{\Phi}{k_B E_{iz}} \frac{\ln(I_0)/I}{T_S} \tag{3.18}$$

Here $\mathcal{N}(E_F)$ describes the density of electron states per unit cell at the Fermi level, $\Phi$ is the work-function, $m_e^*/m$ the electron effective mass to particle mass

ratio, $E_{iz}$ the particle energy normal to the surface and $\frac{\ln(I_0/I)}{T_S}$ being the Debye Waller exponent obtainable from the slope of Debye Waller measurements (see also section 5.2.1).
To apply this method to the case of surfaces of degenerate semiconductors it has to be adapted by considering that the phonon induced modulation of the surface charge density only involves electrons near the surface within the Thomas-Fermi screening length [21].

## 3.8 Inelastic Scattering

For inelastic scattering the imping particle transfers energy from or to the surface by interacting with a quasi particle like a phonon or plasmon. In this work the main focus lies on the creation and annihilation of surface phonons.

### 3.8.1 Surface Phonons

Phonons are quasi particles, describing the quantized lattice vibrations of a crystal. In quantum mechanics these lattice vibrations are described by the Hamiltonian of a harmonic oscillator. With an angular frequency of $\omega$ and the quantum number $l$, the phonon energy is given by:

$$E_l = \left(l + \frac{1}{2}\right)\hbar\omega \tag{3.19}$$

Physical properties of a material like the heat capacity as well as the thermal conductivity are related to the possible phonon states.

At the surface of a crystal new vibrational modes arise. Their origin can be from bulk-phonons, projected to the two dimensional Brillouin zone of the surface as well as new localized surface modes coming from the broken translational invariance.
These surface phonons are described by the vector $\mathbf{Q} = (q_x, q_y)$ and show wavelike characteristics, travelling parallel to the surface. Perpendicular to the surface, their amplitude decays quickly into the bulk.
The three dimensional bulk modes $(\mathbf{Q}, q_z)$ are projected from the bulk to the surface, like seen in the dispersion relation in figure 3.4. Their frequency or energy is in general located above the surface phonons.
Since surface atoms exhibit fewer neighbours in comparison to atoms in the bulk, an alteration of the force constants occurs. This force softening can affect several

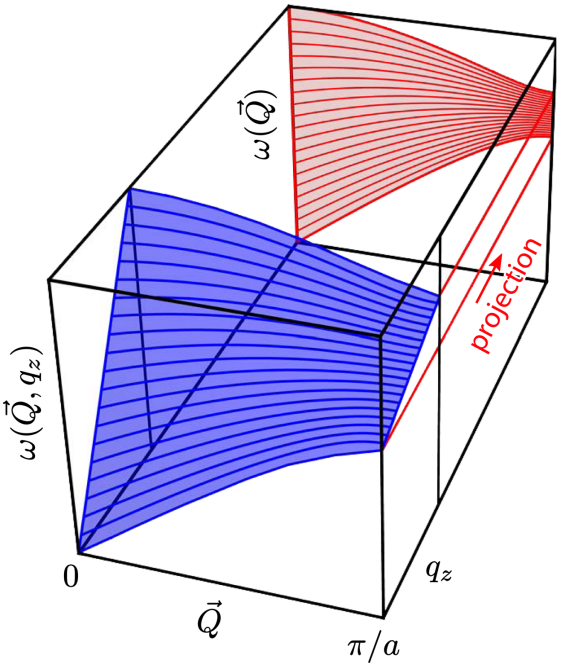


Figure 3.4: Phonons from the bulk are projected onto the surface. The 3-dimensional dispersion curves for parallel **Q** and different $q_z$ from the bulk are converted to two dimensions on the surface while losing their z-variety [9].

of the upper layers beneath the surface.
Surface phonons are characterised by three polarisations (see figure 3.5), referring to the sagittal plane. The sagittal plane, in terms of helium atom scattering, is spanned by the incident wave vector $\mathbf{k_i}$ and the surface normal **n**. Looking along high-symmetry directions of the reciprocal surface lattice, phonons oscillating in the sagittal plane are either called shear-vertical polarized if their displacement is mainly perpendicular to their propagation direction or longitudinal with the displacement mainly in propagation direction. Polarisation in the surface plane with the displacement perpendicular to the sagittal plane is called shear horizontal.
In this work experiments were run exclusively in the plane of high symmetry directions, i.e. the scattering plane and the sagittal plane coincide. In this case phonons with shear horizontal polarisation can not be excited.

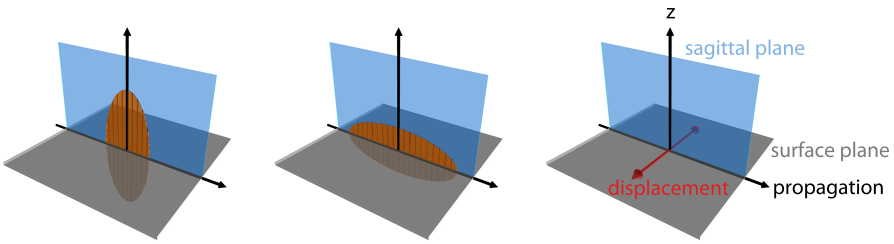


Figure 3.5: There are three types of polarisation for surface phonon modes [22]: (a) Shear vertical: oscillation perpendicular to the propagation direction (transverse), parallel to the sagittal plane. (b) Longitudinal: Polarisation also in the sagittal plane, but oscillation in propagation direction. (c) Shear horizontal: displacement in the surface plane.

## 3.9 Time of Flight Measurement

In time of flight (TOF) measurements, the time $t$ it takes for a particle or particle packets to travel a certain distance $L$ is observed, so its velocity $v$ can be determined:

$$v = \frac{L}{t}. \tag{3.20}$$

It is important to distinguish between particle packets, to later be able to assign a flight time to them. This is accomplished by a so called chopper disk (section 2.1.2).
A more sophisticated approach is the use of a pseudo random chopper disk (section 3.9.2). The flight path starts at the chopper disk and ends at the ionization zone at the detector. Depending on their velocity, faster particles will arrive in shorter time than slower propagating ones. This way a flight time distribution $g(t)$ is obtained, which further allows the calculation of the velocity $f(v)$ and energy distribution $f(E)$ (section 3.9.4).
The intensity of the arriving particles at the detector is stored by a multichannel analyser in the form of a time histogram.

### 3.9.1 Resolution and Correction of TOF Measurements

The resolution of a TOF spectrum, i.e. the width of its peaks, is limited by the velocity spread of the atom beam, as well as the uncertainty of the TOF measurement.
The chopper cuts the incident beam with a frequency $\nu_{chop}$ described by a chopper transmission function $C(t)$, which ideally would exhibit a delta form. Due to

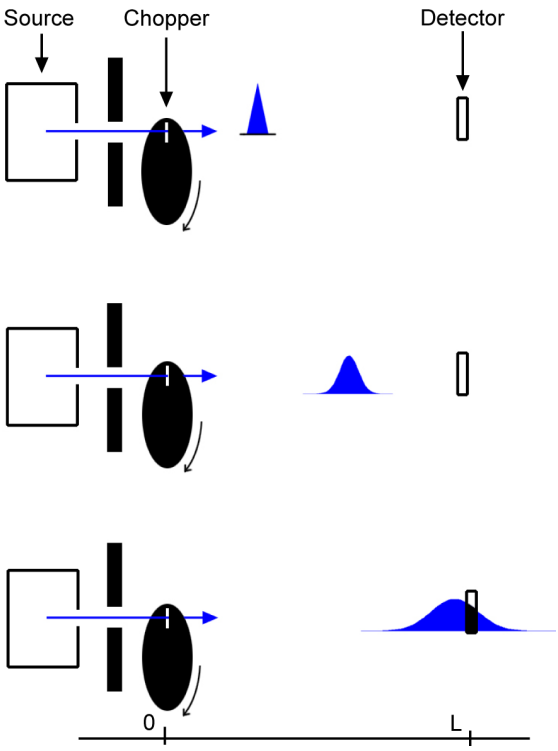


Figure 3.6: The continous beam is separated into small particle packets by the chopper disk. Upon propagation to the detector the packets disperse, due to the velocity spread of the beam [23].

the finite slit width of the chopper disk, $C(t)$ usually shows a trapezoidal shape. Moreover the resolution is constrained by the finite ionisation length of the detector, which adds an uncertainty $D(x)$ to the flight length $L$, since the point of ionisation can not be indicated exactly. Both uncertainties are taken together in an effective transmission function $T_{eff}(t)$ [24].
From experimental measurements, the TOF distribution $G(t)$, affected by both uncertainties, is determined. It can be written mathematically in the form of the convolution integral:

$$G(t) \propto \int_{-\infty}^{\infty} T_{eff}(t-\tau)g(\tau)d\tau \tag{3.21}$$

Both functions $G(t)$ and $T_{eff}(t)$ can be approximated by a Gaussian function. The deconvolution of equation 3.21 provides the real TOF distribution $g(t)$, which also exhibits a Gaussian form.
The time of flight measurement is triggered by an optical impulse from a slit on the rotating chopper disk, starting the multichannel analyser. To compensate for the triggering delay [9], the peak time $t_p$ needs to be corrected by $t_c$ (which is a function of the chopper rotation frequency) to obtain the real flight time $t_f$:

$$t_f = t_p - t_c \tag{3.22}$$

To improve the signal noise ratio many TOF spectra are integrated over several hours by the multichannel analyser.

### 3.9.2 Pseudo Random Chopper

While using a chopper disk to run TOF experiments, a part of the helium beam is blocked and does not participate in the scattering processes, resulting in a significant decrease of intensity. To gain high resolution a very short opening time of the chopper, i.e. a narrow slit width is necessary. To increase the amount of particles transiting the chopper, inserting as many slits on the disk as possible, is a good approach.
Due to the velocity spread of the beam, the passing particle packets will disperse while propagating (see also figure 3.6). In the case of several slits arranged near to each other, the time intervals between two packets may be shorter than the spread between inelastically scattered packets, which causes an overlap of the signal at the detector. A solution to this problem is the use of a so-called pseudo random chopper. It will modulate the continuous beam in a specific sequence, allowing for a deconvolution of the superposition of the wave packets.
The measured intensity $D(t)$ from the detector consisting of a background signal $U(t)$ and the convolution of the wanted TOF distribution $F(t)$ with the known

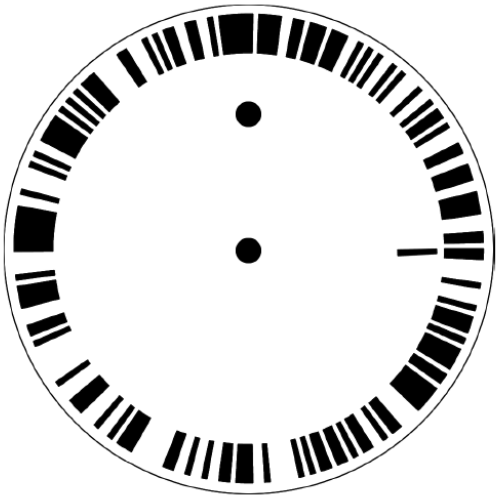

Figure 3.7: Schematic picture of a pseudo random chopper disk [23]. The various slits of different width represent a binary system of "transit" and "blocked" beam.

arbitrary sequence of the chopper $C(t)$, also called shutter function becomes:

$$D(t) = U(t) + (C * F)(t) \tag{3.23}$$

$$D(t) = U(t) + \int C(t - t'')F(t'')dt''. \tag{3.24}$$

To obtain the deconvoluted TOF intensity $F(t)$ from equation 3.23, it is convoluted with the shutter function $C(t)$ [23]. With the constraint of $C(t)$ being a fully random function, its auto correlation function 3.25 is the delta distribution $\delta(\tau)$. The modulation of a beam by this random function and the deconvolution of it, with the same random function is analogous to the modulation with a delta function. With the background $U(t)$ considered as time independent, the cross correlation function (first term in equation 3.26) is achieved.

$$C(t) = \int C(t)C(t + \tau)dt = \delta(\tau) \tag{3.25}$$

$$F(t) = \int C(t')D(t + t')dt' - U \int C(t')dt' \tag{3.26}$$

The cross correlation function further can be evaluated using Fourier transformation, finally yielding the deconvoluted TOF distribution $F(t)$. Since there is no fully uncorrelated random number generator, in an experiment $C(t)$ is realised with a binary pseudo random frequency of slits and teeth on the chopper disk as shown in figure 3.7.

While using the pseudo random chopping technique brings a lot of advantages,

such as an increase in intensity to approximately one half of the initial intensity, it is not useful in cases of huge variation of TOF spectra intensity. The statistical noise of large peaks will spread over the whole spectrum, hiding potentially observable small peaks. Therefore pseudo random chopping should exclusively be applied to TOF experiments, where only peaks of comparable size are expected.

### 3.9.3 Surface Phonon Measurements with TOF

For inelastic scattering an energy transfer between the impinging helium atoms and the probed surface takes place. Surface phonons can either be created by transferring kinetic energy from the helium atom to the surface lattice or annihilated, due to energy transfer from the surface to the probing particle. With the use of TOF measurements, the energy loss or gain from the helium beam can be determined, allowing for a determination of surface phonons and their energies.
Looking at the whole system, energy and momentum conservation also holds for inelastic scattering events. Considering only single phonon events and scattering happening only in the sagittal plane, the conservation of energy can be written as:

$$E_f = E_i + \Delta E = E_i \pm \hbar\omega, \tag{3.27}$$

with $E_i$ being the incident energy, $\Delta E$ the energy exchange by creating or annihilating a phonon with energy $\hbar\omega$ and $E_f$ the final energy after the scattering process. By expressing the energy in terms of the wave vector equation 3.27 can be rewritten as:

$$\frac{\hbar^2}{2m}k_f^2 = \frac{\hbar^2}{2m}k_i^2 \pm \hbar\omega. \tag{3.28}$$

The conservation of parallel momentum is expressed by:

$$\mathbf{K}_f = \mathbf{K}_i + \Delta\mathbf{K}. \tag{3.29}$$

$\Delta\mathbf{K}$ describes the change of parallel momentum of a scattered helium atom. For an incident plane perpendicular to the surface the relation 3.30 can be derived. In this context, see also figure 3.8.

$$k_f \cdot \sin(\theta_f) = k_i \cdot \sin(\theta_i) + \Delta K \tag{3.30}$$

The combination of conservation of energy 3.7 and conservation of momentum 3.30, leads to an expression of total change of energy $\Delta E$ of the scattered particle and thus the phonon energy.

$$\frac{\Delta E}{E_i} + 1 = \frac{\sin(\theta_i)^2}{\sin(\theta_f)^2}\left(1 + \frac{\Delta K}{K_i}\right)^2 \tag{3.31}$$

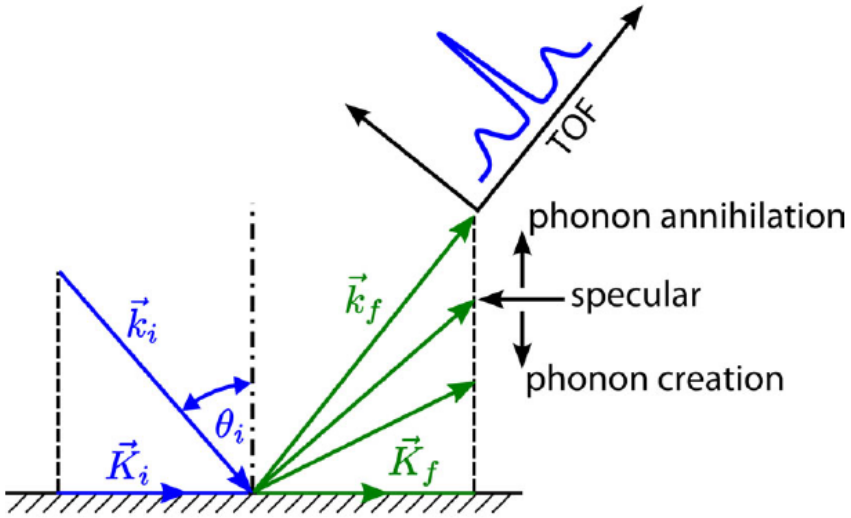


Figure 3.8: Illustration of scattering events with phonon creation and annihilation. In case of elastic scattering (specular), the modulus of the incident and final wave vector stay the same [9].

Rearranged in favour of the momentum transfer:

$$\frac{\Delta K}{K_i} + 1 = \frac{\sin(\theta_f)}{\sin(\theta_i)} \sqrt{\frac{\Delta E}{E_i} + 1} \tag{3.32}$$

Equation 3.31 is also referred to, as the scan curve for inelastic scattering of atoms from a surface. The scan curve defines the possible energy $\Delta E$ and momentum $\Delta K$ of a surface phonon, which can be seen under a certain incident angle $\theta_i$ and incident energy $E_i$ in scattering experiments. Through variation of $\theta_i$ a wide range of $\Delta K$ is accessible. This way the surface phonon dispersion over the whole Brillion zone can be measured (see also figure 3.9).

The sign of the change of energy $\Delta E$ determines, if a phonon was created (negative $\Delta E$) or annihilated (positive $\Delta E$). Depending on the phonon propagating parallel to $K_i$ or anti parallel to $K_i$, the change of parallel momentum is either positive or negative.

### 3.9.4 From Time of Flight to Energy Scale

With the goal to determine the surface phonon dispersion, the phonon energy $\Delta E$ has to be calculated from the measured TOF spectra. The kinetic energy of a

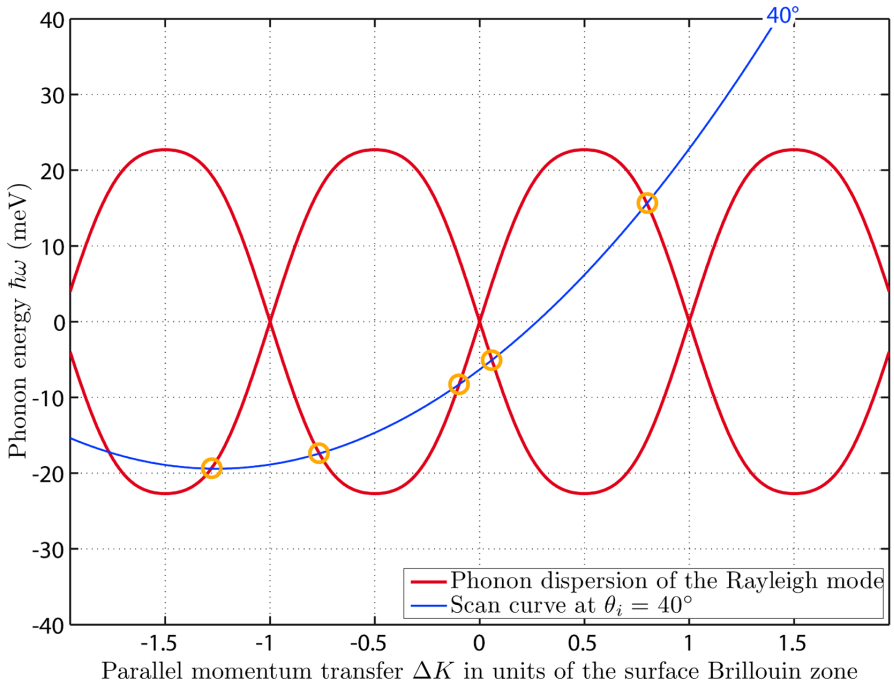


Figure 3.9: Example of a scancurve (blue) of a helium scattering experiment [9] and the phonon dispersion (red). Possible phonon events can occur at the intersections of the scan curve and the dispersion curve (orange circles).

particle can be written in the simple form of equation 3.33.

$$E = \frac{m}{2}\left(\frac{length}{TOF}\right)^2 \tag{3.33}$$

Remembering the relation 3.27, the phonon energy is the energy difference $\Delta E$, before and after scattering. Since the kinetic energy of the helium particle will not change before hitting the surface, i.e. during the flight path from the chopper to the sample, the relevant flight distance is the one from the surface (or target) to the detector $L_{TD}$. Therefore the final energy $E_f$ can be expressed by:

$$E_f = \frac{m}{2}\left(\frac{L_{TD}}{t_{TD}}\right)^2 \tag{3.34}$$

with $t_{TD}$ being the flight time of inelastically scattered helium atoms from the target to the detector. Obviously the flight time from the chopper to the target $t_{CT}$ is the same, no matter if the particle will scatter elastically or inelastically. Therefore $t_{CT}$ can be substituted from the known TOF of elastically scattered atoms $t_e$, based on their total flight distance from chopper to detector $L_{CD}$. Subtracting the expression for $t_{CT}$ from the total flight time $t_{CD}$ gives then $t_{TD}$:

$$t_{TD} = t_{CD} - \frac{L_{CT}}{L_{CD}} t_e \tag{3.35}$$

The total flight distance from chopper to detector as well as the distance from the target to the detector are well known for the used apparatus [9]. Therefore the TOF spectra can be transformed to energy according to equation 3.36:

$$\Delta E = E_f - E_i = E_i \left[\left(\frac{\frac{L_{TD}}{L_{CD}} t_e}{t_{CD} - \frac{L_{CT}}{L_{CD}} t_e}\right)^2 - 1\right] \tag{3.36}$$

Note that equation 3.36 provides a non-linear relation between energy and TOF. To maintain the correct intensity after the transformation from TOF to energy, the signal has to be scaled by its Jacobian 3.37, which effects the height and the width of the peaks in the energy spectrum as seen in figure 3.10.

$$\left|\frac{dt_{TD}}{d\Delta E}\right| = \frac{t_{TD}^3}{m \cdot L_{TD}^2} \tag{3.37}$$

Noise and intensity increase on the creation side, while the peaks get flattened out on annihilation side.
As already mentioned phonon processes are only observable at intersections of the scan curve and the phonon dispersion curve. Because of the velocity spread, the scan curve is broadened. Hence the angle at which the scan curve interacts with the dispersion is crucial for the sharpness of the observable peak. Best results are achieved for an angle of 90°. With angles getting smaller, peaks will get broader, with the worst case being a tangential intersection, which also results in an effect called kinematical focusing, which can appear in elastic measurements ($\theta$-scans) and can be misinterpreted as selective adsorption resonances [25].

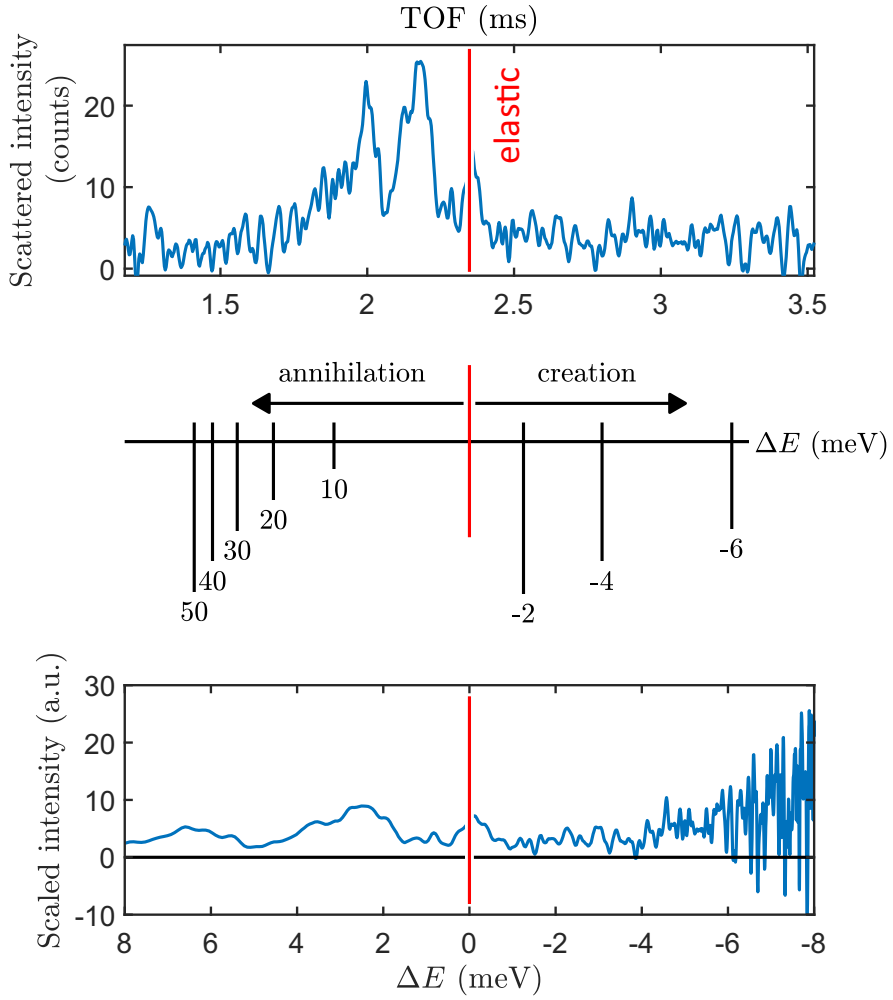


Figure 3.10: This figure shows an example of the transformation from a TOF spectrum (top) to energy (bottom) by applying equation 3.36 and 3.37. The middle graph shows the non-linearity of the transformation. Due to the scaling, the intensity gets flattened out on the annihilation side (bottom graph left) and the noise at creation side (negative $\Delta E$) is enhanced, noticeable with increasing oscillations of intensity. This measurement was taken for $Sb_2Te_3(111)$ along $\overline{\Gamma K}$ with an incident energy of $E_i = 10.13\,\text{meV}$ under an angle of $\theta_i = 45°$.

# 4 Antimony Telluride $Sb_2Te_3$

Antimony telluride ($Sb_2Te_3$) is a prominent p-type semiconductor and multifunctional material, well known for its outstanding thermoelectric properties at room temperature [2] and is used in power generation, heat pumping and cooling applications. Approaches to further improve thermoelectric efficiency in low dimensional systems [26–28] and the contribution of topological surface states to thermoelectric properties have been investigated by Hinsche *et al* [29]. $Sb_2Te_3$ also plays a major roll in phase change memory alloys [30] and sparked interest in the field of topological insulators [3, 31, 32].

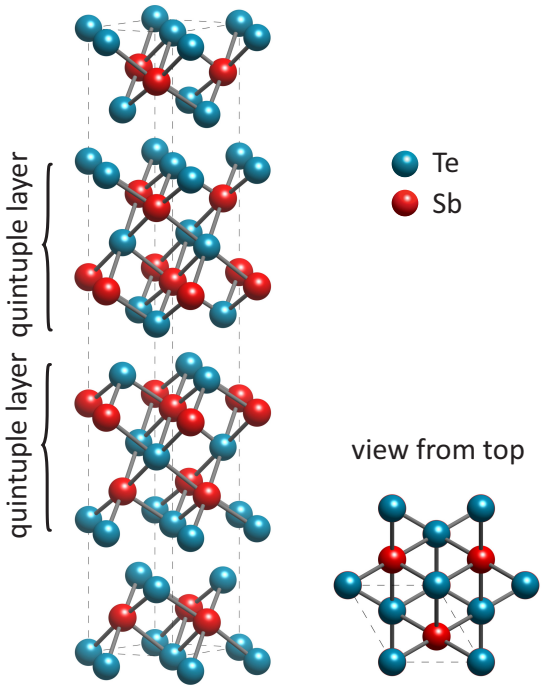


Figure 4.1: The left panel shows the crystal structure of three quintuple layers of $Sb_2Te_3$, with the top view on the right. The dotted lines indicate the conventional hexagonal unit cell.

Antimony telluride has a rhombohedral crystal structure, which can also be described with a hexagonal unit cell as seen in figure 4.1 together with the hexagonal surface unit cell in the (111) plane. The material consists of five atomic

layer sheets, arranged along the z-direction (perpendicular to the surface), known as quintuple layers. Each quintuple layer consists of two equivalent tellurium atoms, two equivalent antimony atoms and a third tellurium atom. The bonding is strong between the atomic layers within a quintuple layer but much weaker, predominantly of the van der Waals type, between two quintuple layers.
With a cut through the (111) plane of the rhombohedral unit cell, the uppermost atomic layer on the surface boundary consists of tellurium, followed by an antimony layer and so forth. Hence the helium atoms in HAS experiments are primarily interacting with the electron cloud of the tellurium atoms.

## 4.1 Topological Insulator and $Sb_2Te_3$

Topological insulators are classified as a new quantum state of matter, which exhibit an insulating electronic band gap in the bulk and gapless topologically protected conducting states on the surface. These states arise from the combination of spin-orbit interaction and time-reversal symmetry. Two-dimensional topological insulators like graphene [33] or HgTe/CdTe quantum well structures, which are described in terms of quantum spin hall states, show the properties of spin splitting propagation, meaning spin and momentum of a particle are correlated [34]. For three-dimensional topological insulators, one can imagine stacked layers of two-dimensional quantum spin hall insulators.
Besides the well investigated binary compounds $Bi_2Se_3$ and $Bi_2Te_3$, $Sb_2Te_3$ has been confirmed to be a three-dimensional topological insulator with a single Dirac cone on the surface [3]. The topological surface states [35] of three-dimensional topological insulators close the band gap and form a Dirac cone with linear dispersion as illustrated in figure 4.2. The surface electronic band structure of $Sb_2Te_3$ has been well investigated in recent years experimentally by (time resolved) angle resolved photo emission spectroscopy (ARPES) [5, 7, 36] and theoretically. It has been shown for $Sb_2Te_3$, in contrast to other topological insulator materials like $Bi_2Se_3$ and $Bi_2Te_3$, that the Dirac point at the intersection of the surface states, is located well above the Fermi level in the bulk band gap [4, 6], due to natural p-doping in the as-grown crystals. Therefore $Sb_2Te_3$ is not suited for prospective applications in spintronic devices. However, it has been shown that the Fermi level can be shifted above the Dirac point, without changing the band structure, by n-doping with Cs [37].
Further, depending on the position of the Fermi level, a possible hole pocket has been predicted in the $\overline{\Gamma M}$ high symmetry direction of the surface Brillouin zone, from *ab-initio* calculations as seen in figure 4.3. This pocket possibly can be observed as satellite peaks in the diffraction pattern of helium atom scattering [18]. Due to the Dirac point of $Sb_2Te_3$ naturally being above the Fermi level, the initial states on the upper and lower Dirac cone are unoccupied. Additionally the

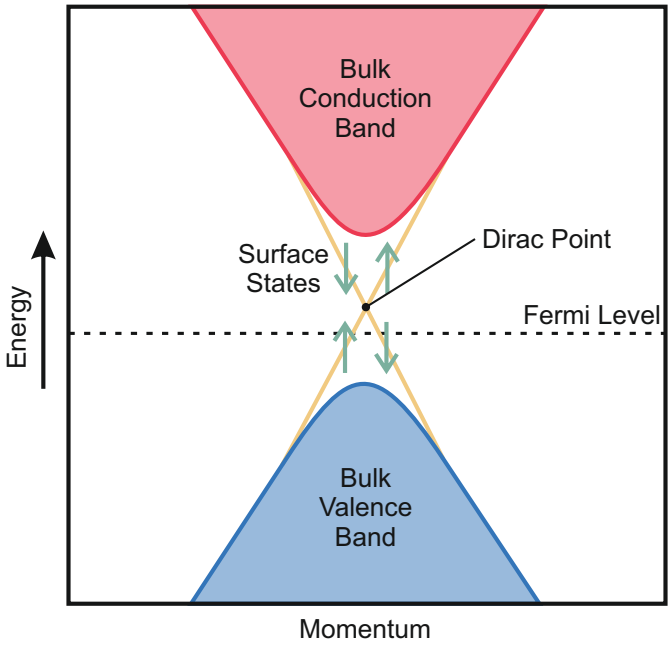


Figure 4.2: Sketch of the electornic band structure of a topological insulator. In this case, the Dirac point, defined by the intersection of the expansion (yellow) of the conduction and valence band, is located above the Fermi level, as it is expected for $Sb_2Te_3$.

Dirac cone surface states are separated from the bulk valence band, hence unoccupied states of the Dirac cone can be independently investigated in time resolved ARPES measurement [36].

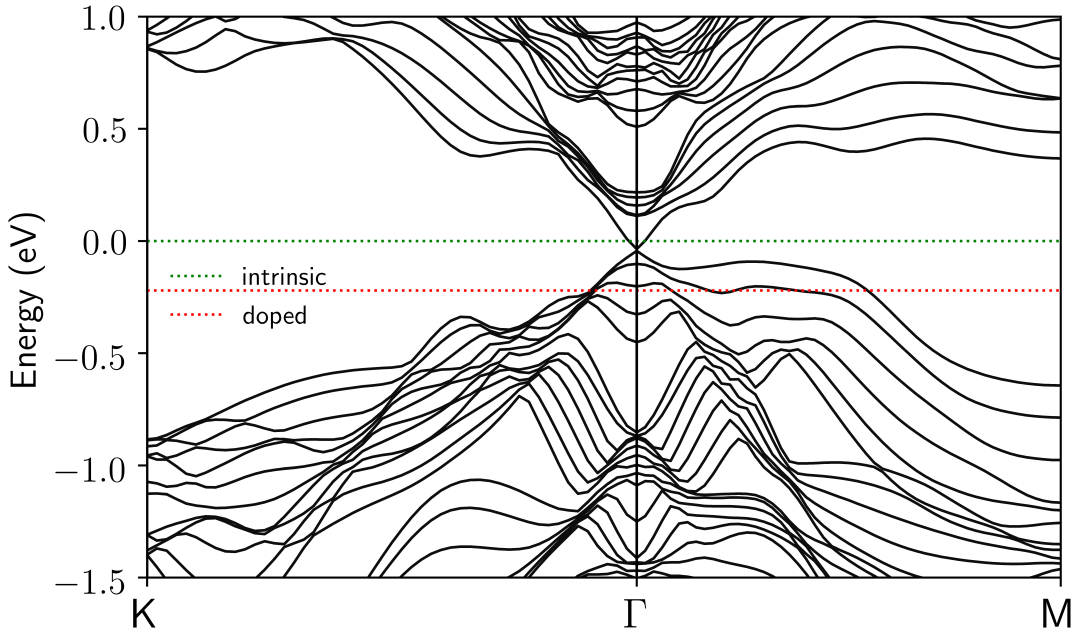


Figure 4.3: Calculated surface band structure of $Sb_2Te_3$ with the Dirac cone visible at the Γ point. A possible narrow hole pocket occurs in $\overline{\Gamma M}$ -direction, depending on the position of the Fermi level. The "intrinsic" line (green) indicates the Fermi level for the undoped crystal, whereas the "doped" line (red) shows the expected Fermi level for a naturally grown crystal, which turns out to be p-doped, beneath the Dirac point.

## 4.2 Sample Fabrication and Preparation

The sample which was probed within the framework of this thesis, was synthesized by a research group at the university of Aarhus at the chemistry department. The phase purity has been measured by X-ray diffraction and unit cell parameters have been extracted with the Rietveld method. The crystal was formed by slow cooling the melt in a quartz tube. Afterwards it was cleaved along the (111) plane as seen in figure 4.4. For the measurements a drop sized sample was sticked onto a sample plate with epoxy resin. To obtain a clean surface, the sample was prepared by the so-called scotch tape method. The uppermost layers of the sample gets exfoliated by attaching scotch tape to it and carefully peeling it off afterwards. This process has to be be repeated several times. The last exfoliation is done under high vacuum conditions in the load lock chamber, before the sample is stored in the sample mounting of the main chamber, to ensure minimal surface contamination. Additionally, before running scattering experiments, the composition of the sample

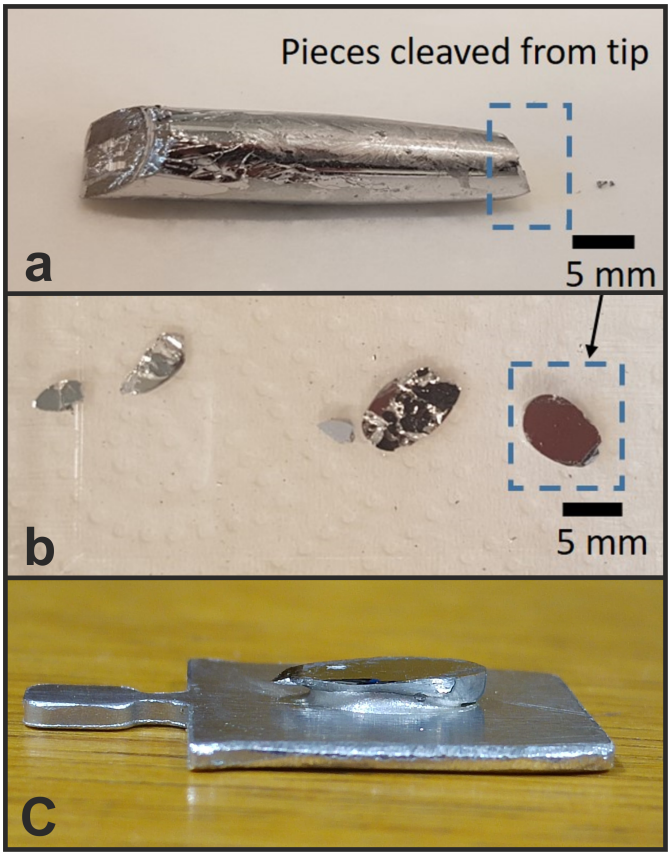


Figure 4.4: (a) Sample of $Sb_2Te_3$, grown from the melt. (b) Cleavage from the crystal tip in the (111) plane. (c) Prepared sample piece fixed on sample carrier for mounting into the main chamber of the helium atom scattering apparatus.

has been analysed by Auger electron spectroscopy. The received spectrum can be seen in figure 4.5, which shows significant intensities at the expected energies, when compared to spectra from literature [38], for pristine antimony and tellurium.

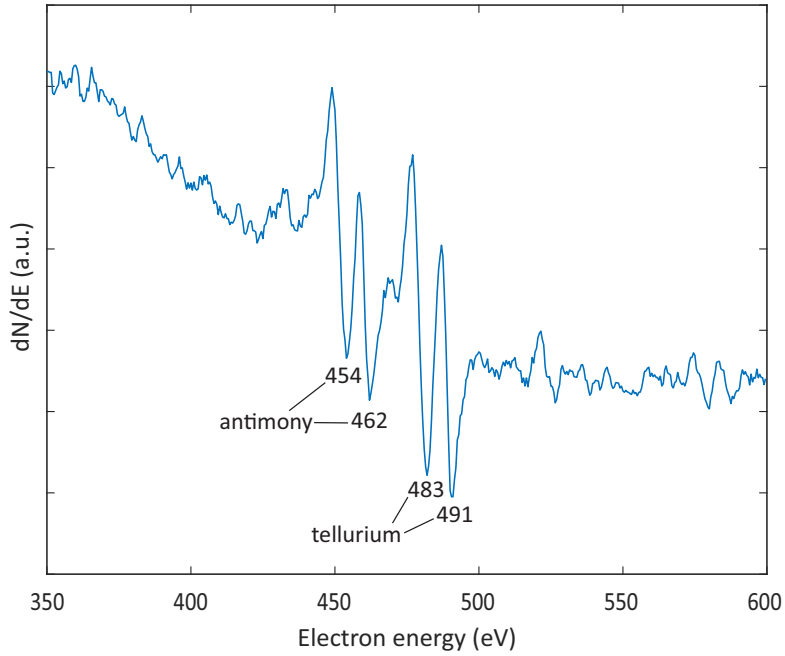


Figure 4.5: Auger electron spectrum of the $Sb_2Te_3$ sample. Compared to MN-transitions found in literature [38], significant peaks at 454 and 462 eV can be assigned to antimony and at 483 and 491 eV to tellurium.

# 5 Elastic Scattering on $Sb_2Te_3$(111)

## 5.1 LEED

The apparatus used in this work for HAS experiments, is equipped with a low energy electron diffraction (LEED) device. With a new sample mounted in the main chamber, at first the orientation of the sample has to be clarified by LEED, before further fine adjustment can be done. By varying the azimuthal angle of the sample holder, the crystal can be arranged in the wanted high symmetry direction $\overline{\Gamma M}$ or $\overline{\Gamma K}$. Figure 5.1a shows a picture of the fluorescent screen of the LEED. The

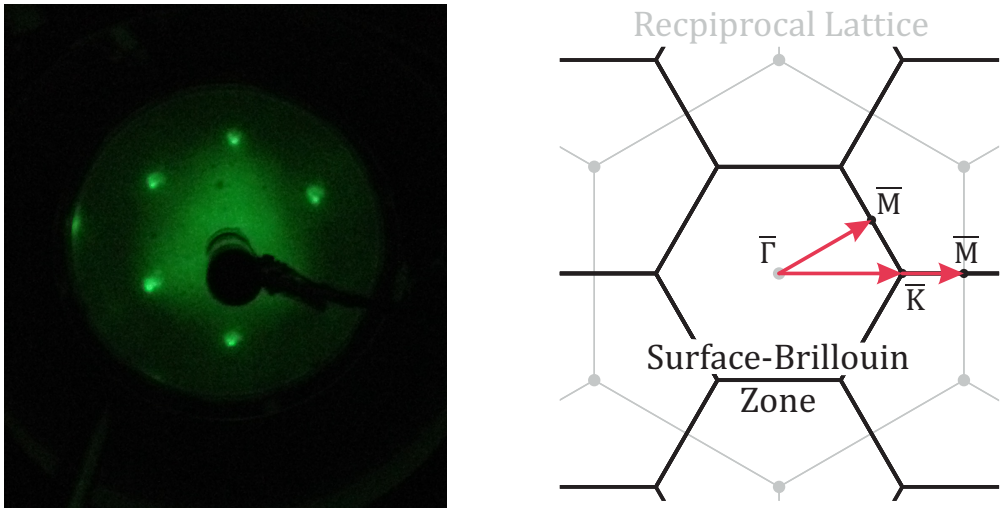


(a) (b)

Figure 5.1: (a) Picture of the LEED-fluoroscopic screen showing the reciprocal lattice of the $Sb_2Te_3$ sample. The sample is orientated in $\overline{\Gamma K}$ direction regarding the incident helium beam from the left. (b) High symmetry direction $\overline{\Gamma M}$ and $\overline{\Gamma K}$ of the surface Brillouin zone (black), constructed from the reciprocal lattice (grey).

6 spots on the screen represent the first order diffraction from elastically scattered electrons corresponding to the reciprocal lattice of the crystal, with a part of the second order already visible on the left edge of the screen. The zeroth order is

covered by the electron gun in the center of the screen. With the helium beam approaching from the left side, in the case of figure 5.1a, the sample is arranged in the $\overline{\Gamma K}$ -direction of the surface Brillouin zone, which is sketched in figure 5.1b.

## 5.2 Elastic Helium Atom Scattering on $Sb_2Te_3(111)$

From the results of elastic scattering measurements the sample properties can be investigated. These scans are important for further analysis and characterisation. To perform an elastic measurement, the incident helium beam energy $E_i$ and temperature of the sample $T_S$ are kept constant, while the incident angle $\theta_i$ is changed in small steps to scan through the wanted angular range, by rotating the sample (see also chapter 2). As described in section 3.5, for specific angles at which diffraction is expected, peaks can be seen in the intensity spectrum of a $\theta$-scan. In figure 5.2 an example of a $\theta$-scan in $\overline{\Gamma K}$ direction is shown with visible first order peaks to the left and right of the centered specular peak. Diffraction peaks will get closer to the specular peak with increasing incident energy. For the current sample and experimental parameters, in $\overline{\Gamma K}$ direction only diffraction peaks up to the first order were visible, since higher orders are out of the possible scanning range of the $\theta$ angle. For $\theta$-scans in $\overline{\Gamma M}$ direction, diffraction peaks could be seen up to second order. From the distance of the diffraction peaks with respect to the centered specular peak, it is possible to determine the lattice constant for the investigated crystal, with the use of the equations from section 3.5.

The average lattice constant $a$ for $Sb_2Te_3$ was evaluated by averaging over several $\theta$-scans in $\overline{\Gamma M}$ and $\overline{\Gamma K}$ direction. The lattice constant has been determined for two different surface temperatures $T_s$, at room temperature at 23 °C to $a = (4.242 \pm 0.006)$ Å as well for a cooled sample with $T_S$ = -160 °C to $a = (4.225 \pm 0.006)$ Å. As expected the lattice constant becomes smaller at lower temperatures. Assuming a linear thermal expansion behaviour, the expansion coefficient can be estimated by

$$\alpha = \frac{1}{L}\frac{dL}{dT} \tag{5.1}$$

to $\alpha = (2.2 \pm 0.8) \cdot 10^{-5}$ $K^{-1}$, compared to the linear expansion obtained in the bulk from X-ray diffraction with $\alpha = (1.8 \pm 0.6) \cdot 10^{-5}$ $K^{-1}$ at 270 K [39]. All results for the lattice constant are in good agreement compared to values obtained from other works, as listed in table 5.1.

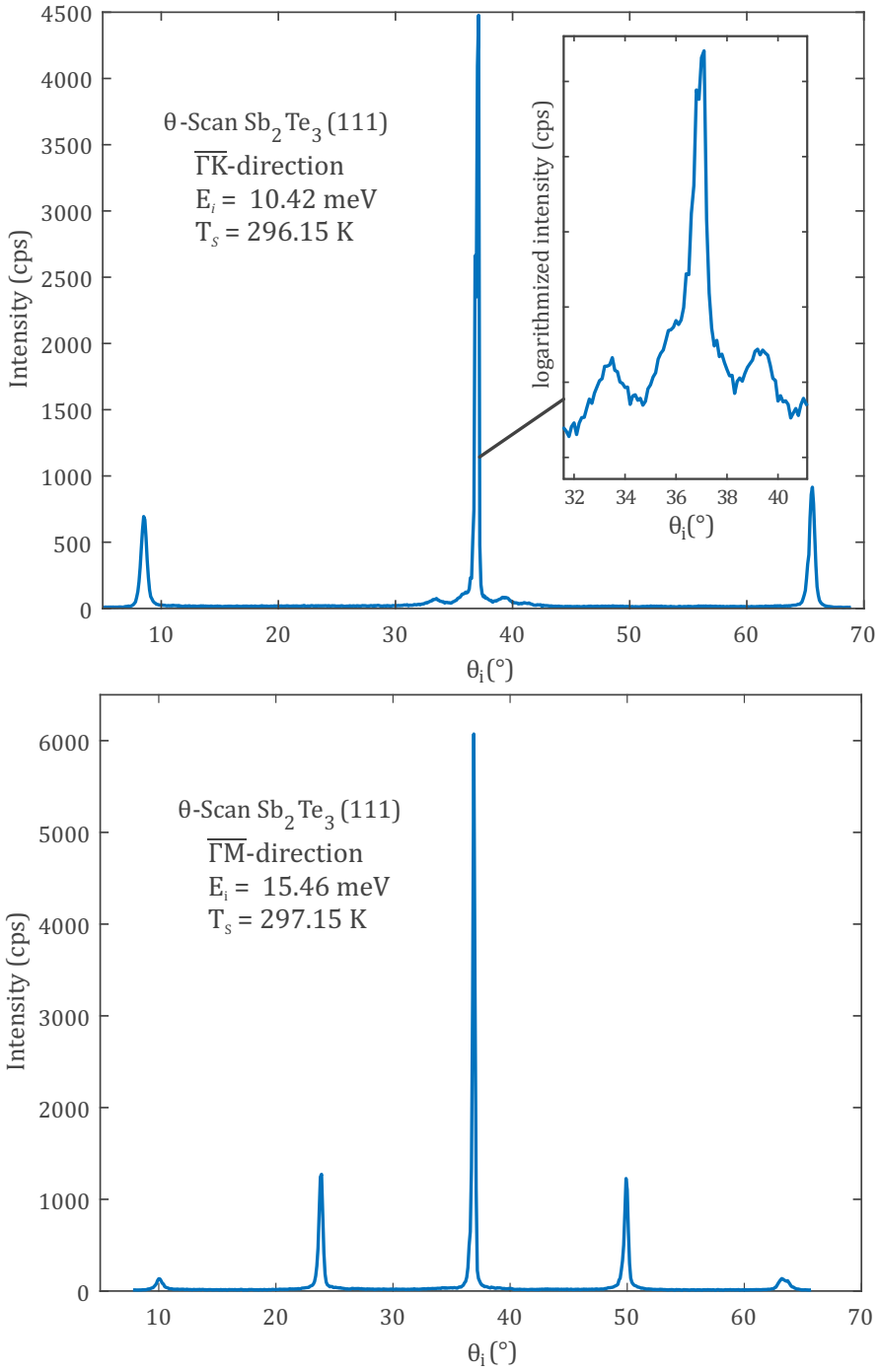


Figure 5.2: Examples of elastic scattering measurements ($\theta$-scans), scanning through a range of incident angles $\theta_i$, in the $\overline{\Gamma K}$ (top) and $\overline{\Gamma M}$ direction (bottom). In the center, the specular peak exhibits the highest intensity. To the left and the right of it, diffraction peaks of first order and second order (only $\overline{\Gamma M}$ ) can be seen. The insert in the top panel shows a close-up of the specular peak on a logarithmic scale, which makes two possible satellite peaks visible.

Table 5.1: Values for the lattice constant $a$ of $Sb_2Te_3$ obtained from $\theta$-scans with helium atom scattering (HAS) from this work, compared to values from other works, obtained by X-ray diffraction (XRD) and electron diffraction analysis (EDA).

| | a (Å) | $T_S$ (K) |
|---|---|---|
| HAS | 4.242 ± 0.006 | 296 |
| HAS | 4.225 ± 0.006 | 113 |
| XRD [40] | 4.2691 | 295 |
| XRD [39] | 4.2423 | 0 |
| XRD [41] | 4.264 | 302 |
| EDA [42] | 4.25 | - |

### 5.2.1 Debye-Waller Factor

As mentioned in 3.7, the amount of inelastic scattering events highly depends on the surface sample temperature. In figure 5.3 the scattering intensity at the specular angle at $\theta_i = 45.75°$ has been measured, while the sample temperature $T_S$ increases in several steps from 113 K to 323 K. With increasing temperature, the rate of inelastic scattering events become more and more dominant in relation to elastic scattering events, which gives rise to a decreased signal at the zeroth order diffraction peak (specular peak). Beside the specular peak a shoulder on its right side shows up. This could be a hint for a selective adsorption resonance (section 3.6). To clarify this, several more scans with varying incident energy $E_i$ would be necessary, which was not part of this work.
From the set of measurements, the maximum intensity for each temperature was evaluated. Since the $\theta$ angle can only be changed in finite discrete steps, it is possible to "miss" the real maximum intensity. For this reason, the data points were fitted with Gaussian functions ($1\sigma$ confidence interval) for each temperature, which in most cases gave a better estimation for the intensity maxima. In figure 5.4 the natural logarithm of the ratio of all temperature dependent maxima $I(T_S)$ is obtained this way, with the extrapolated intensity $I_0$ at $T_S = 0$ K. $\ln(\frac{I(T_S)}{I_0})$ was then fitted linearly over the temperature range. Taking all done measurements into account, the intensity tends to deviate a little bit from the linear behaviour, since the Debye-Waller approximation no longer holds at higher temperatures. All maxima are located beneath the fitting line above a certain temperature, however this behaviour is not very noticeable in the chosen example in figure 5.4. Also the adjustment and calibration usually happen at the lowest temperature. Due to thermal expansion of the sample, mounting and manipulator parts, with increasing temperature, it is possible that the tilt angles etc. shift out of the optimum position, resulting in an additional elastic intensity decrease. From the slope of the linear fit, the in section 3.7 discussed Debye-Waller factor was calculated as $2W(T_S) = -(4.57 \pm 0.18) \cdot 10^{-3}\ \mathrm{K}^{-1}$. Knowing the Debye-Waller factor, the surface

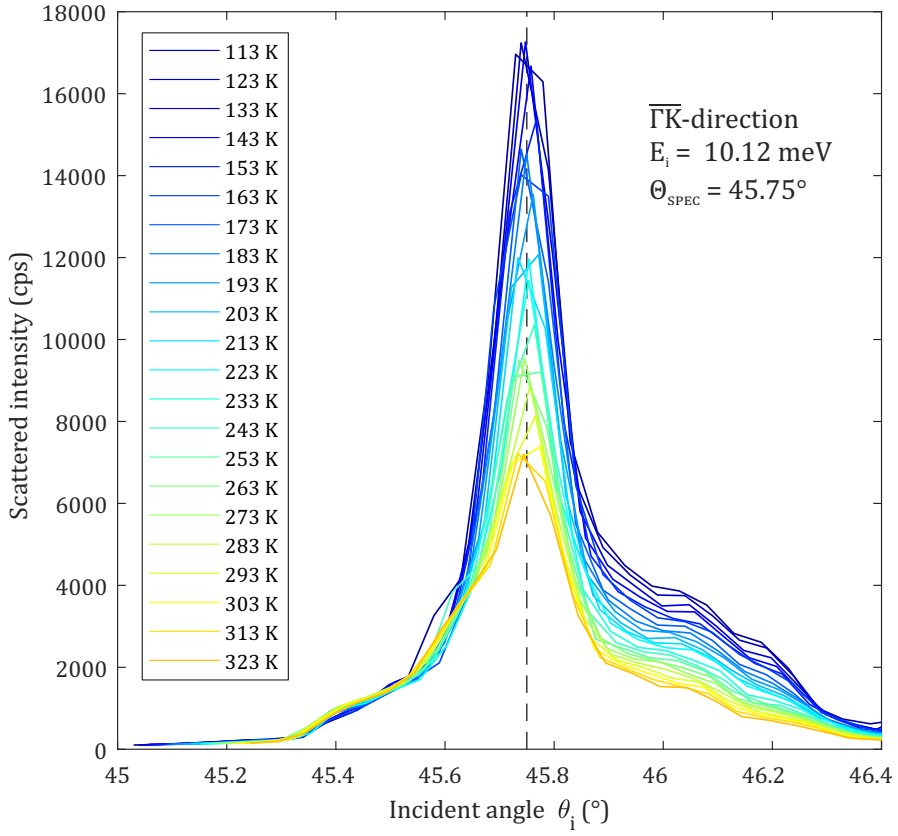


Figure 5.3: Attenuation of intensity in terms of the surface temperature at the specular angle for $Sb_2Te_3(111)$, orientated in $\overline{\Gamma K}$ direction. For the measurement the sample was adjusted onto the specular peek for highest intensity.

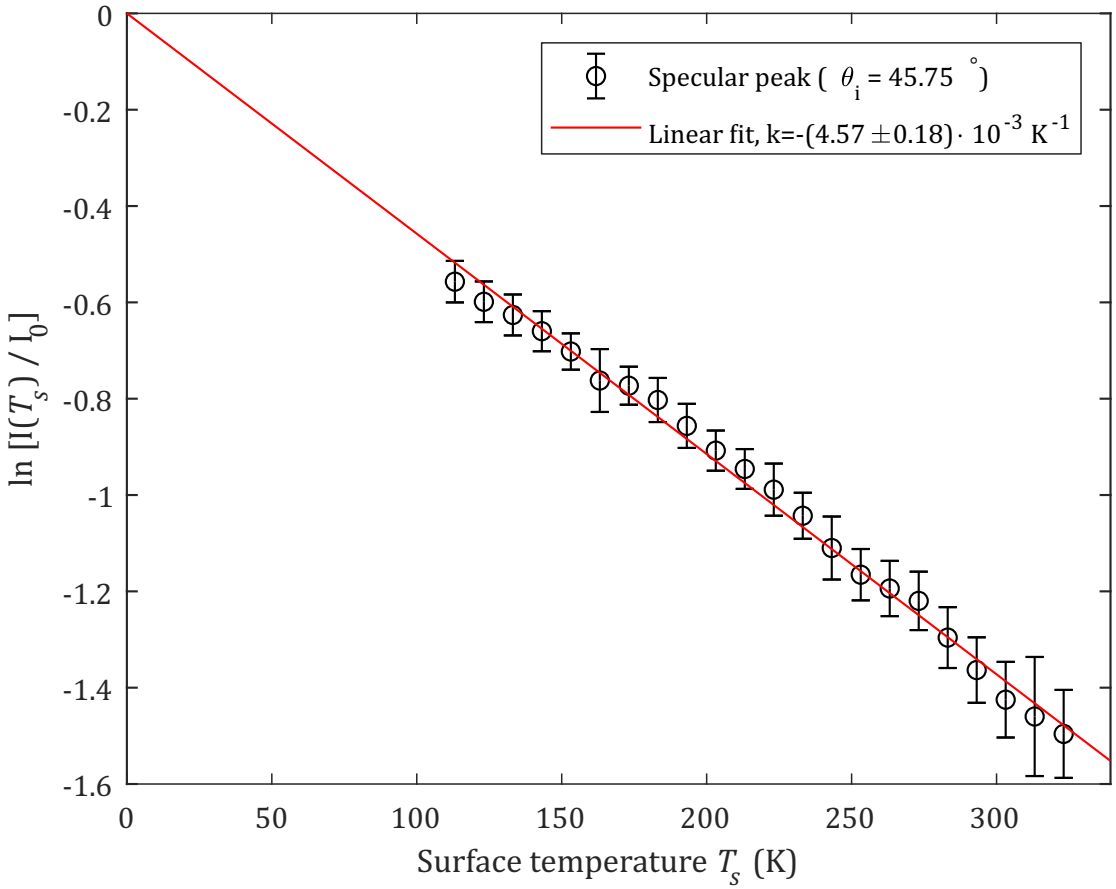


Figure 5.4: This plot shows the logarithm of the intensity maxima (black circles), measured from elastic scattering at the specular condition for different surface temperatures. From the slope of the linear fit (red line) the Debye-Waller factor is determined. With higher surface temperature, the amount of inelastic scattered particles increases, leading to a thermal attenuation of the specular peak.

Debye-temperature $\theta_D$ can be determined from equation 3.17. The incident energy $E_i$ and angle $\theta_i$ are known from the measurement setup. The potential well depth has been calculated by analysing selective adsorption events from elastic scattering measurements (not part of this work), as it was done for $Bi_2Se_3(111)$ [43], with $D = 5.43\,\text{meV}$. The effective mass of the surface atoms $M$, in a first attempt can be estimated by the mass of the upper most layer of tellurium with an atomic mass $m_{Te} = 127.4\,\text{u}$, leading to a surface Debye-temperature of:

$$\theta_D = (141 \pm 3)\text{K}. \tag{5.2}$$

This result is located between the element specific bulk Debye-temperaturs for tellurium with 157 K and antimony with 135 K for the $Sb_2Te_3$ compound, both obtained from the density of phonon states by nuclear inelastic scattering [40], 200 K from X-ray powder diffraction [39] and a value from literature $\theta_D = 160\,\text{K}$ [44] for $Sb_2Te_3$. Since the incoming helium atom does not interact only with the electrons of the upper atom layer but with the layers below those by electron-phonon interaction, especially the second layer consisting of antimony ($m_{Sb} = 121.76\,\text{u}$), has to be considered for a better approach, which would lead to a significant higher effective mass. Since the effective mass can not be determined exactly, a more useful parameter is given with the relation $\alpha = \theta_D^2 \cdot M$. Inserted into equation 3.17 this gives:

$$\alpha = \frac{12m(E_i \cos^2(\theta_i) + D)}{k_B k} \tag{5.3}$$

with k being the slope of the linear fit from figure 5.4, a value $\alpha = (4.19 \pm 0.17) \cdot 10^{-21}\,\text{K}^2\,\text{kg}$ is obtained for $Sb_2Te_3$ (111), which is significantly larger than for $Bi_2Se_3$ $\alpha = (1.69 \pm 0.09) \cdot 10^{-21}\,\text{K}^2\,\text{kg}$ [11].

### 5.2.2 Electron-Phonon-Coupling

As described in section 3.7.1, the Debye-Waller exponent $2W(T_S)$ can be used, to derive the mass enhancement factor $\lambda$, indicating the strength of electron phonon coupling for a conducting surface [45, 46]. The Debye-Waller factor $2W(T_S)$ written in terms of the electron phonon coupling $\lambda$ can be seen in the following equations:

$$\lambda = \frac{\pi}{2n_s} \cdot \gamma \tag{5.4}$$

$$\gamma = \frac{\Phi}{A_c k_{iz}^2 k_B} \frac{\partial \ln I(T_S)}{\partial T_S}. \tag{5.5}$$

With the partial derivation $\frac{\partial \ln I(T_S)}{\partial T_S}$ being the Debye-Waller exponent from the previous section 5.2.1, $\phi = 4.45\,\text{eV}$ the work function [28], $A_c = 15.64\,\text{Å}^2$ the unit

cell area. $c_0 = 10.15\,\text{Å}$ is the thickness of the quintuple layers of $Sb_2Te_3$ with the factor 2, for two metallic sheets in it. The perpendicular part of the incident wave vector $k_{iz} = 3.07\,\text{Å}^{-1}$ can be determined from the scattering geometry and the incident energy $E_i$. The number of metallic layers contributing to the phonon-induced modulation of the surface charge density is taken into account by $n_S$, which is estimated by

$$n_S = \frac{2\lambda_{TF}}{c_0}. \tag{5.6}$$

Therefore the Thomas-Fermi screening length $\lambda_{TF}$ was calculated referring to [47] (for Gauss units):

$$\lambda_{TF} = \left(\frac{\hbar^2\epsilon_r}{4e^2m^*}\right)^{1/2}\left(\frac{\pi c_0}{3n_c}\right)^{1/6}. \tag{5.7}$$

Here $\epsilon_r = 115$ [48] is the relative permittivity for $Sb_2Te_3$, $m^* = 0.095 \cdot m_e$ [49] the effective electron mass and $n_c = 5.67 \cdot 10^{13}$ [49] the surface charge carrier concentration in $\text{cm}^{-2}$, to $\lambda_{TF} = 44\,\text{Å}$. Further by inserting into equation 5.4, the electron-phonon coupling constant $\lambda = 0.29$ is obtained.
Due to the large electronic corrugation leading to a hard wall potential, a Beeby correction [19] (section 3.7) needs to be applied to $k_{iz}^2$:

$$k_{iz}'^2 \coloneqq k_{iz}^2 + \frac{2m_{He}D}{\hbar^2} \tag{5.8}$$

with $m_{He}$ the mass of helium and $D = 5.43\,\text{meV}$ the already used potential well depth from section 5.2.1, the coupling constant (with a relative uncertainty of about 10 %) becomes:

$$\lambda = 0.14 \tag{5.9}$$

which is smaller than for $Bi_2Se_3(111)$ with $\lambda = 0.23$ and $Bi_2Te_3(111)$ $\lambda = 0.19$ [50], on the other hand it is the same order of magnitude in particular when compared to $Bi_2Te_2Se(111)$, where in absence of quantum well states a value of $\lambda = 0.08$ was obtained. So far no other work considering the electron-phonon coupling constant for $Sb_2Te_3$ is available (to the best of my knowledge), to which the obtained results could be compared.

# 6 Inelastic Scattering on $Sb_2Te_3$(111)

This section mainly covers the time of flight measurements done for $Sb_2Te_3$(111) and their analysis to obtain the surface phonon dispersion and compare the results with the theoretically calculated dispersion from density functional perturbation theory [51].

## 6.1 Time of Flight Measurements

For this work, several time of flight measurements were taken for $Sb_2Te_3$(111), with the sample orientated in $\overline{\Gamma K}$ and $\overline{\Gamma M}$ direction, for various incident energies of the helium beam and different surface temperatures. The incident angles have been chosen for a full coverage of the whole Brillouin zone in terms of the associated scan curve, as well to an angular range with high enough signal intensity. The latter was mainly the case for incident angles between the specular angle and the $\pm$ first order diffraction angles. For each measurement at a certain incident angle, the signal from the multi channel analyser was deconvoluted and transformed into energy scale (see also section 3.9.4) leading to an energy transfer spectrum as shown as an example in figure 6.1. This measurement was taken in $\overline{\Gamma K}$ direction, at fixed nozzle temperature, for an incident energy of $E_i = 10.13\,\text{meV}$ and at an incident angle of $\theta_i = 51.25°$. The peak at the vertical dotted line represents defuse elastically scattered particles at $\Delta E = 0\,\text{meV}$. The grey line represents the deconvoluted TOF signal, after the non-linear transformation to energy, which results in high oscillations on the phonon creation side (negative $\Delta E$) and flattening on the annihilation side (positive $\Delta E$). Due to the increasing oscillation at higher energies, for phonon creation events ($\Delta E < 0$) only peaks up to an energy of about $\Delta E$ = -6 meV have been considered. Events below this value could hardly be identified, since they could not be distinguished from the noise. Further for phonons on the annihilation side above 12 meV, due to Bose-Einstein distribution, phonon occupation decreases to a level, where there is too low intensity to identify any distinct peaks.
To account for the non-equal spacing on the x-axis and for better identification of

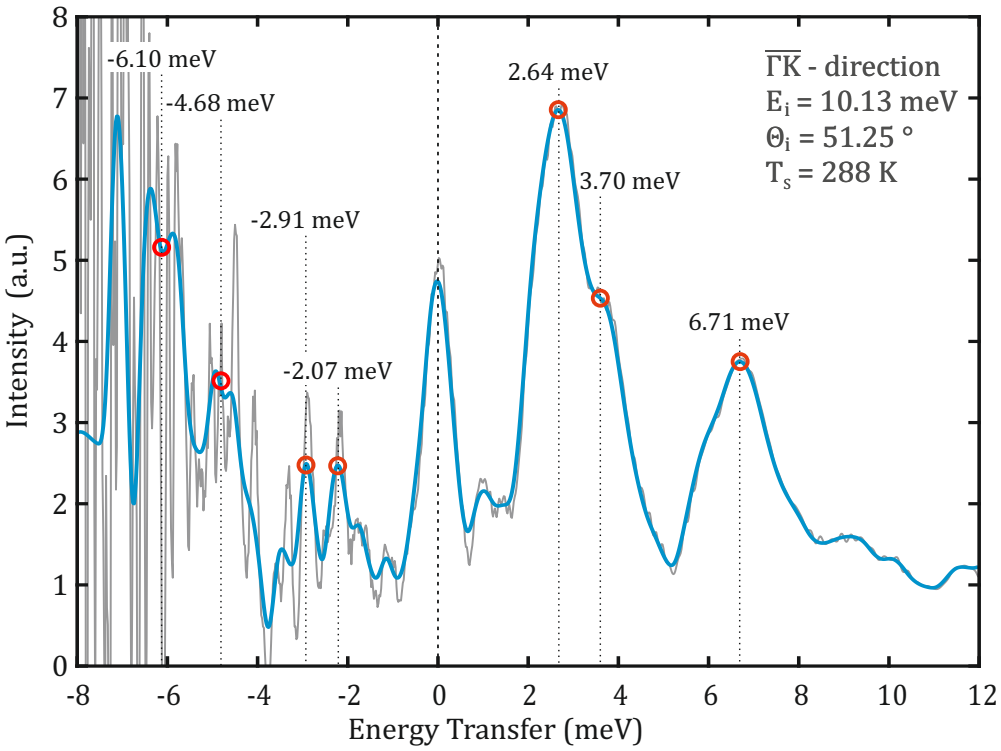


Figure 6.1: Energy transfer spectrum from a TOF measurement. The grey curve shows the deconvoluted TOF spectrum, transformed into energy, which was smoothed by binning (blue curve). Significant peaks are marked with red circles, together with their corresponding energies.

phonon events, the curve was smoothed by binning (blue curve).
Phonon events with significant intensity are marked with a red circle and the associated energy transfer above. The peak evaluation has been performed manually, since identifying significant peaks was not always possible from a single spectrum, so other spectra needed to be considered as well, looking at how those peaks evolve under different incident angles or energies. Although a numerical approach for automated peak scanning was attempted, results were not reliable enough and improving the script was not possible in reasonable time for this work.

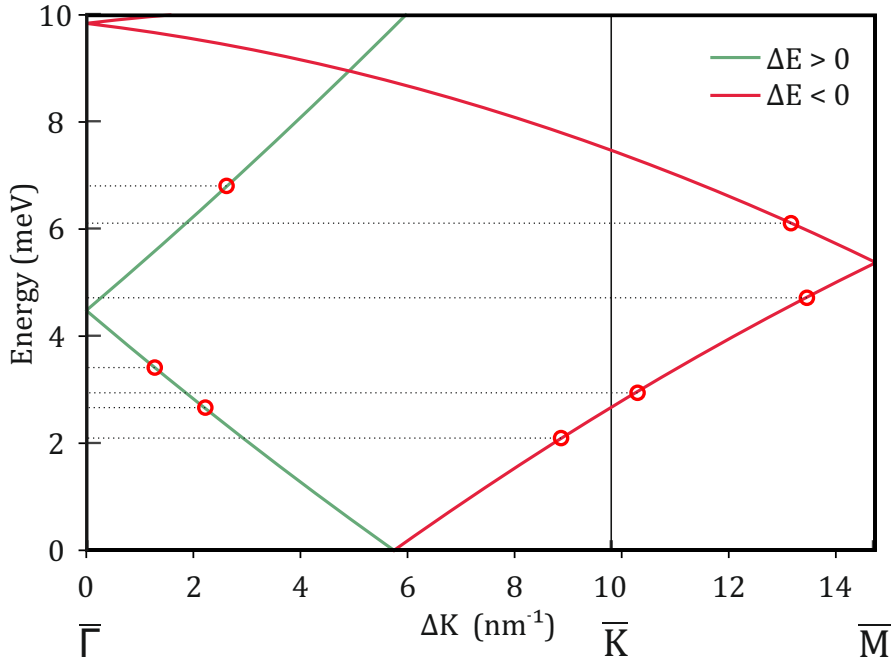


Figure 6.2: Scan curves for the incident angle of the measurement, shown in figure 6.1. The green curve represents positive energy transfer and red negative. The scan curves have been folded back at the border of the Brillouin zone. The red circles mark the intersections of the peak energies found in figure 6.1 with the scan curve. The related momentum can be read form the x-axis.

In figure 6.2 the corresponding scan curve for the related incident angle $\theta_i$ and incident energy $E_i$ of this measurement is plotted from equation 3.32 for energy versus phonon momentum corresponding to the momentum transfer of the scattered helium particle $\Delta K$ and was folded back into the first Brillouin zone. Additionally the scan curve for negative energies has been folded up to positive energies. Since the phonon dispersion is entirely defined within the first Brillouin zone, all phonon events can be projected back into it. The scan curve for positive energy transfer (phonon annihilation) is drawn in green and the scan curve for negative $\Delta E$ (phonon creation) in red. The corresponding phonon momentum $\Delta K$ is then calculated according to the scan curve for each identified phonon en-

ergy $\Delta E$ ($E_{phonon} = \Delta E$). This procedure has been repeated for all taken TOF measurements.

## 6.2 Elastic Phenomena in Inelastic Measurements

While analysing energy spectra from time of flight (TOF) measurements, under certain conditions, symmetric peaks of unusual high intensity can be observed. The occurrence of such peaks, in many cases, can be associated with elastic diffraction effects rather than inelastic processes and therefore need to be excluded for the analysis of the phonon dispersion [52].
Those so called deceptons originate from the fact, that the velocity distribution of the helium beam has a certain width around the average incident velocity, rather than being a delta distribution. For particle velocities $v'$, which differ from the average velocity $v_0$ of the distribution, the scattering conditions change as well as their TOF:

$$\Delta t_{TOF} = L_{CD} \left( \frac{1}{v_0} - \frac{1}{v'} \right). \tag{6.1}$$

This can be very misleading in terms of TOF energy spectra evaluation, if one is not aware of the possible existence of such decepton peaks. In figure 6.3(a) an example of an energy spectrum from TOF measurements in $\overline{\Gamma M}$ direction features a peak of very high intensity on the phonon annihilation side. If compared to the related scan curve for this measurement 6.3(b), the peak is located pretty close to the theoretically calculated Rayleigh mode [51] and seems like a legit measurement point for the phonon dispersion. Although at first it appears as a peak from a phonon event, the peak comes from a shifted $1^{st}$ order diffraction, due to the velocity spread. Therefore deceptons will not be seen near the specular peak. The scattering angles $\theta_i$, for which the Bragg condition is fulfilled, can be calculated by using equation 3.9, considering the different velocities $v'$, which deviate from $v_0$. The difference in energy $\Delta E$ is given by equation 3.36 with the time of flight being $t_{CD} = \frac{L_{CD}}{v'}$ in this case. Inserting the new $\Delta E$ and $\theta_i$ in the scan curve equation for momentum transfer 3.32, leads to a "quasi" dispersion relation for deceptons as seen in figure 6.4. One can now look at the intersection of this dispersion and the measurement specific scan curve. By comparing the intersection with the position of energy spectra peaks, possible deceptons can be excluded from measurement data for further evaluation.

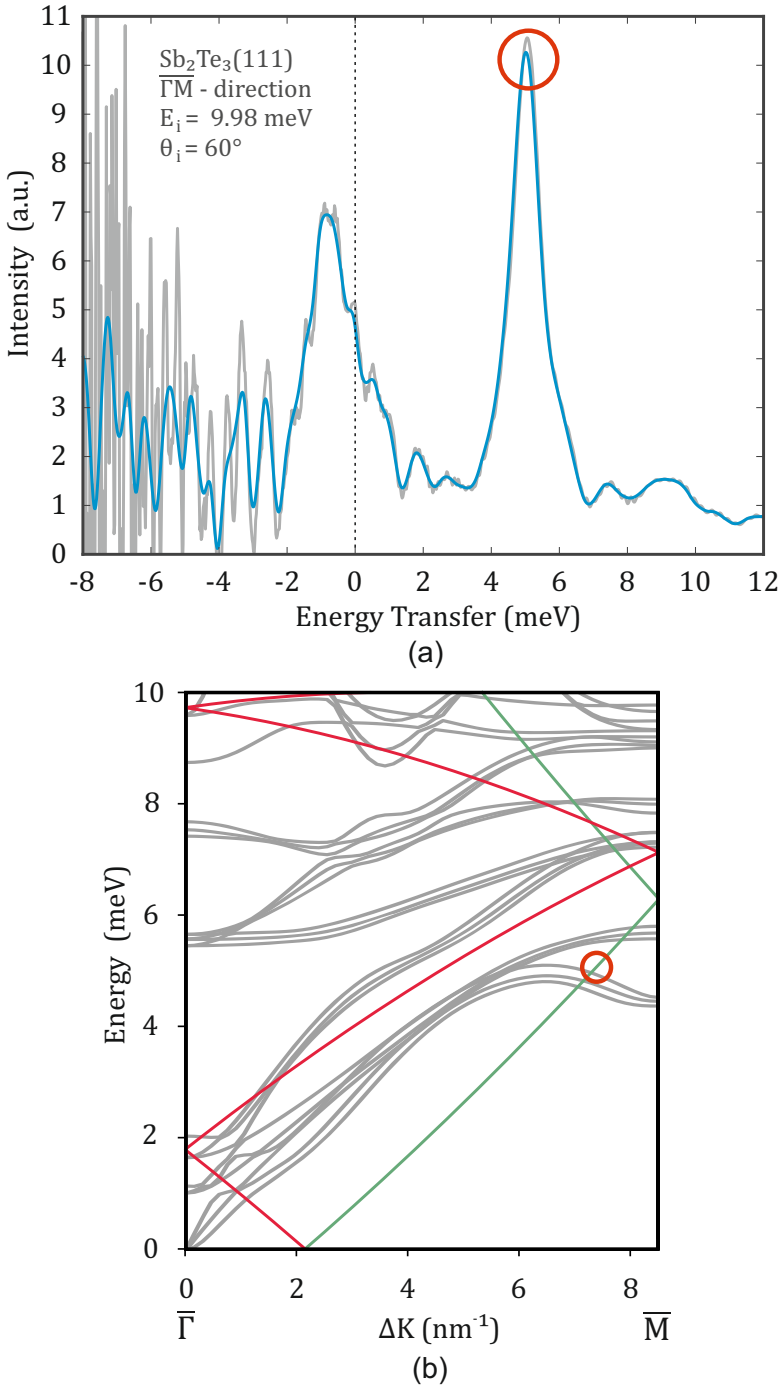


Figure 6.3: Example of a measurement in $\overline{\Gamma\mathrm{M}}$ direction with a decepton appearing in the energy spectrum, with the corresponding scan curve. (a) Energy transfer spectrum from a TOF measurement, which features a suspicious peak (marked with a red circle) with high intensity on the annihilation side on the right. As seen in figure 6.4, this peak can be set into relation with a $G_{\bar{1}0}$ decepton. (b) The related scan curves to (a) with the decepton peak position marked with a red circle and the theoretical calculated dispersion (grey lines).

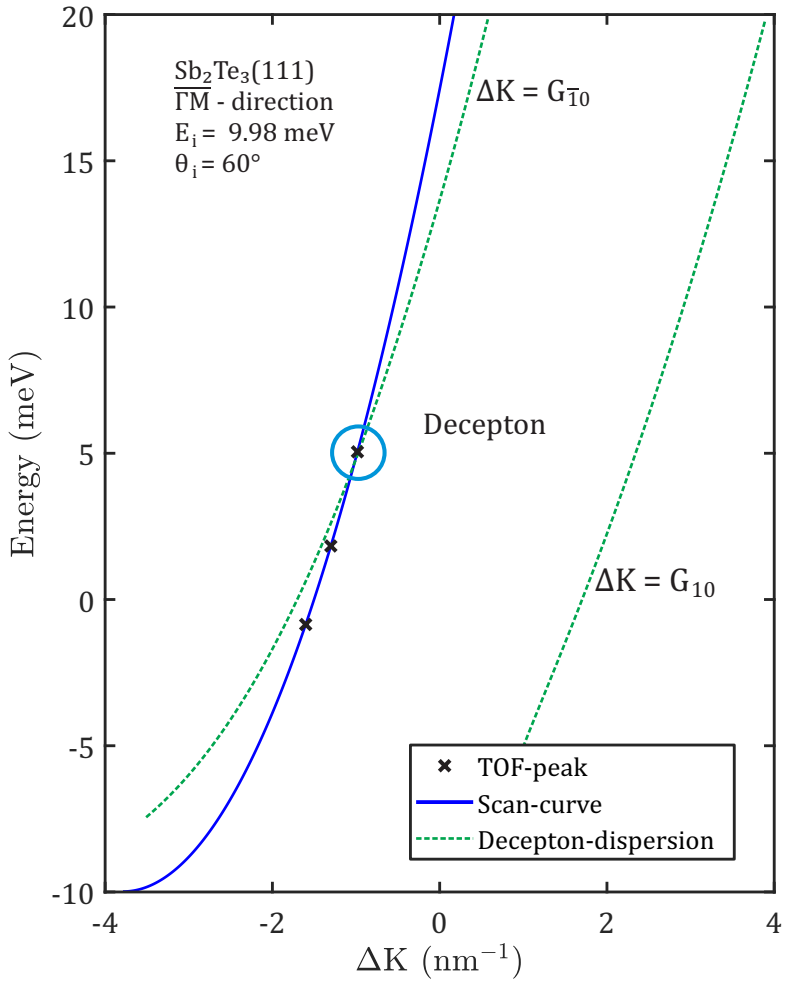


Figure 6.4: This figure shows an example, for how TOF peaks were checked, whether their origin is from a decepton or inelastic scattering. The two "quasi" dispersion curves for deceptons from -1$^{st}$ and 1$^{st}$ order are plotted as green dotted lines, with the scan curve drawn in blue. The black crosses mark the three peaks found in the TOF energy spectrum for this measurement (also see figure 6.3). The peak with highest energy is located very close to the intersection of the scan curve and the decepton dispersion for $G_{\bar{1}0}$, which is an obvious hint, that its related peak originates from a shifted first order diffraction.

## 6.3 Surface-Phonon Dispersion of $Sb_2Te_3(111)$

After evaluation of all TOF measurements as described in section 6.1 and exclusion of the found deceptons, all data points were combined in a single plot. Figure 6.5 represents the whole surface phonon dispersion of $Sb_2Te_3(111)$, achieved experimentally by TOF measurement from helium atom scattering. In general phonon events were easier to measure at lower energies, especially close to the $\overline{\Gamma}$-point with regions of high density of phonon events, where a branch rises from 0 energy (the Rayleigh mode). For higher phonon energies, intensities become rather low, and were more and more hidden in the noise, resulting in fewer detected events. Although a similar count of measurements was taken for both high symmetry directions, for this sample phonons seemed more likely to be detected in $\overline{\Gamma K}$ directions, resulting in a higher amount of data points available in this direction. Noticeable are a number of points at energies below the Rayleigh mode, which will be discussed later.

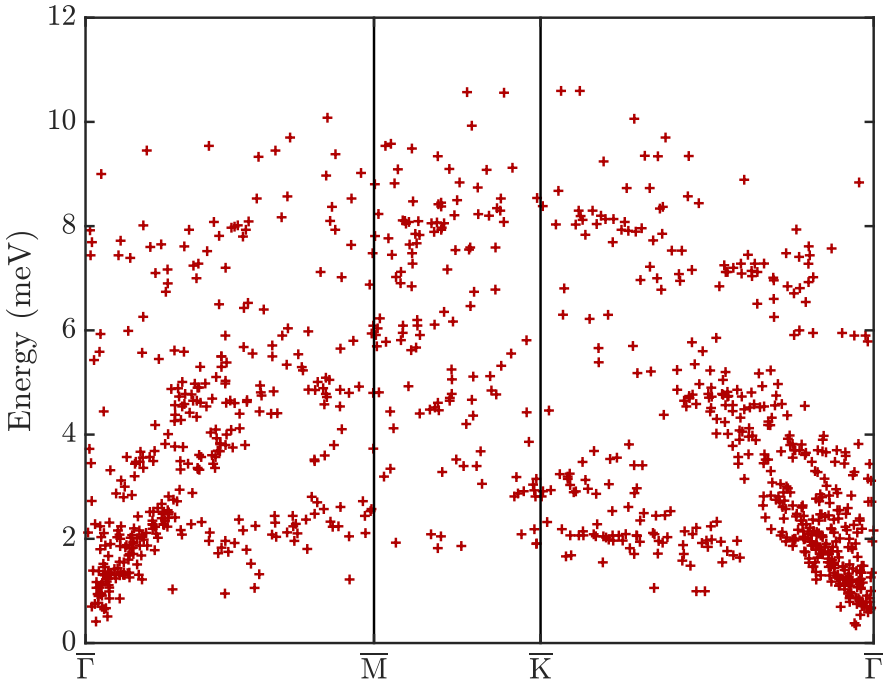


Figure 6.5: Every dot in this figure represents one intensity peak found in the energy transfer spectra, gathered from several TOF measurements for $Sb_2Te_3(111)$, with various incident angles and energies. They are plotted by energy, depending on their momentum in the high symmetry direction $\overline{\Gamma K}$ and $\overline{\Gamma M}$ for the whole Brillouin zone. Noticeable is the high density for lower energies especially at the $\overline{\Gamma}$-point, which correspond to the Rayleigh mode.

## 6.4 Comparison of TOF Data with Theoretical Calculations

So far (to the best of my knowledge) no other experimental data for the surface phonon dispersion of $Sb_2Te_3$, beside $\overline{\Gamma}$-point phonon energy from Raman and infrared spectra [53], is available at the moment. However $ab-initio$ calculations have been performed by Davide Campi, using density functional perturbation theory (DFPT)[51]. The surface phonon dispersion has been calculated for 3 quintuple layers without considering spin-orbit coupling along the symmetry directions $\overline{\Gamma M}$ and $\overline{\Gamma K}$.
The theoretical surface phonon dispersion is shown in figure 6.6. At the $\overline{\Gamma}$-point, the three acoustic phonon modes start with zero energy, with the lowest mode being the Rayleigh mode and various optical modes at higher energies. Every mode does split up in 3 different lines due to the calculation for three quintuple layers, since each additional considered layer, gives rise to a small energy change of the phonon mode. The surface phonon events gathered from TOF energy spectra have

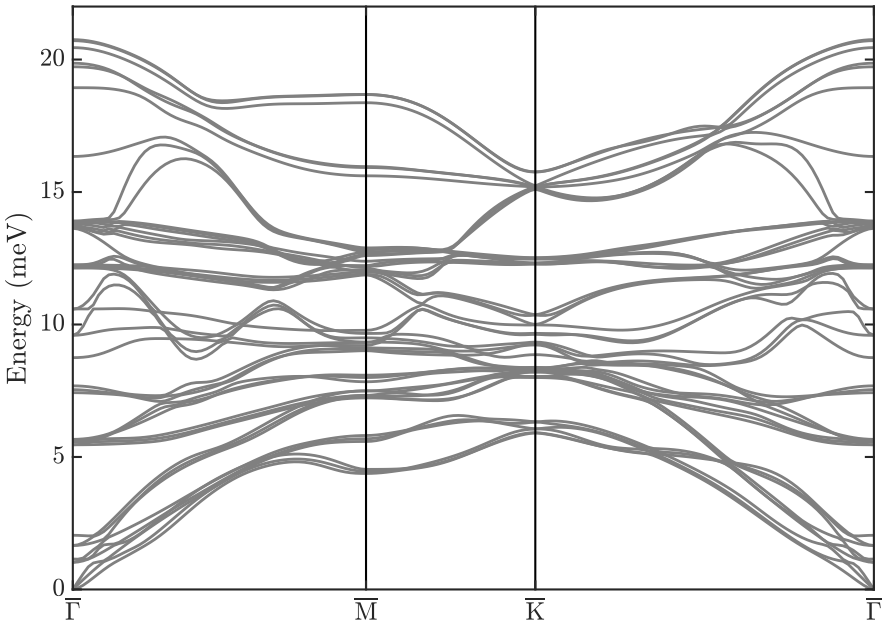


Figure 6.6: Theoretical calculation of the surface phonon dispersion for the first Brillouin zone from DFPT as reported in Davide Campi *et al.* [51].

been compared to the theoretical surface phonon dispersion, as seen in figure 6.7 for the example of the measurement of section 6.1. Therefore all identified peaks from the energy spectrum were transferred to the dispersion relation and plotted together with the theoretical dispersion. To distinguish the different modes, they have been coloured. According to their vicinity to the calculated modes, every phonon event was marked with the mode related colour and tag.

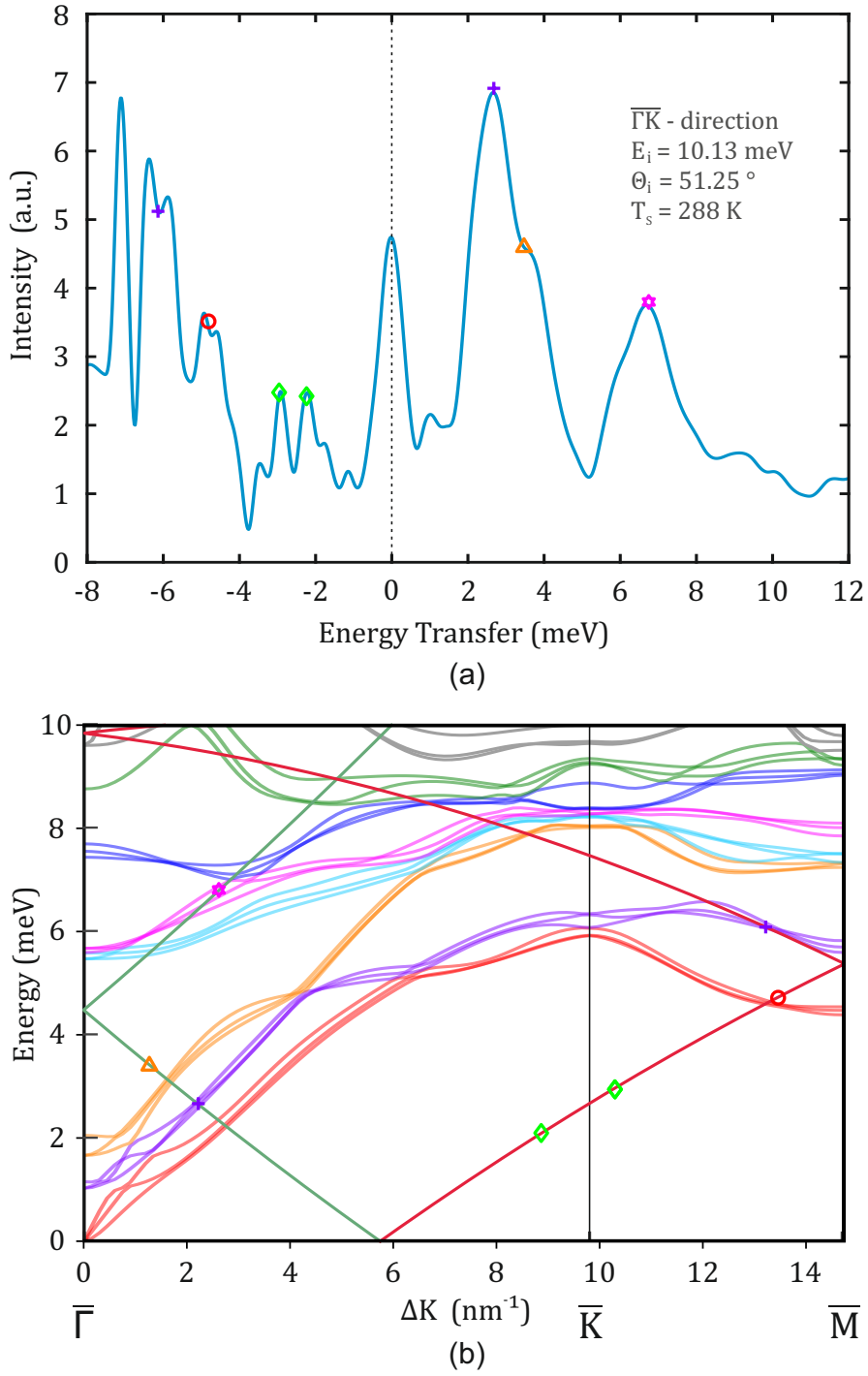


Figure 6.7: By comparing all identified TOF peaks from the energy transfer spectrum (a) to the theoretical dispersion according to the scan curve (b), phonon events can be assigned to their related mode. To easily distinguish between the single modes, they have been coloured differently and peaks have been marked with different tags.

In figure 6.7(b) one can see the scan curve for positive energy transfer (green), intersecting the three acoustic modes, red (Rayleigh mode), purple and orange. These three modes run close to each other in the intersection area, resulting in a high intensity peak on the annihilation side in figure 6.7(a). Due to the peak width of about 2 to 4 meV, the single modes can not be resolved.
At the right side of figure 6.7(b), one can see the negative scan curve cutting the second acoustic mode almost in a tangential way, also leading to a broader peak in the energy spectrum, possibly causing kinematical focusing in elastic measurements [25].
The creation side also features two significant low energy peaks, marked with green diamonds, which can not be assigned to any mode in figure 6.7(b). Those phenomena do not only appear in this single measurement, but can be seen in several others as well. They are also known from other helium atom scattering experiments, investigating similar materials like $Bi_2Se_3$ [46] and will be discussed in more detail in section 6.6.

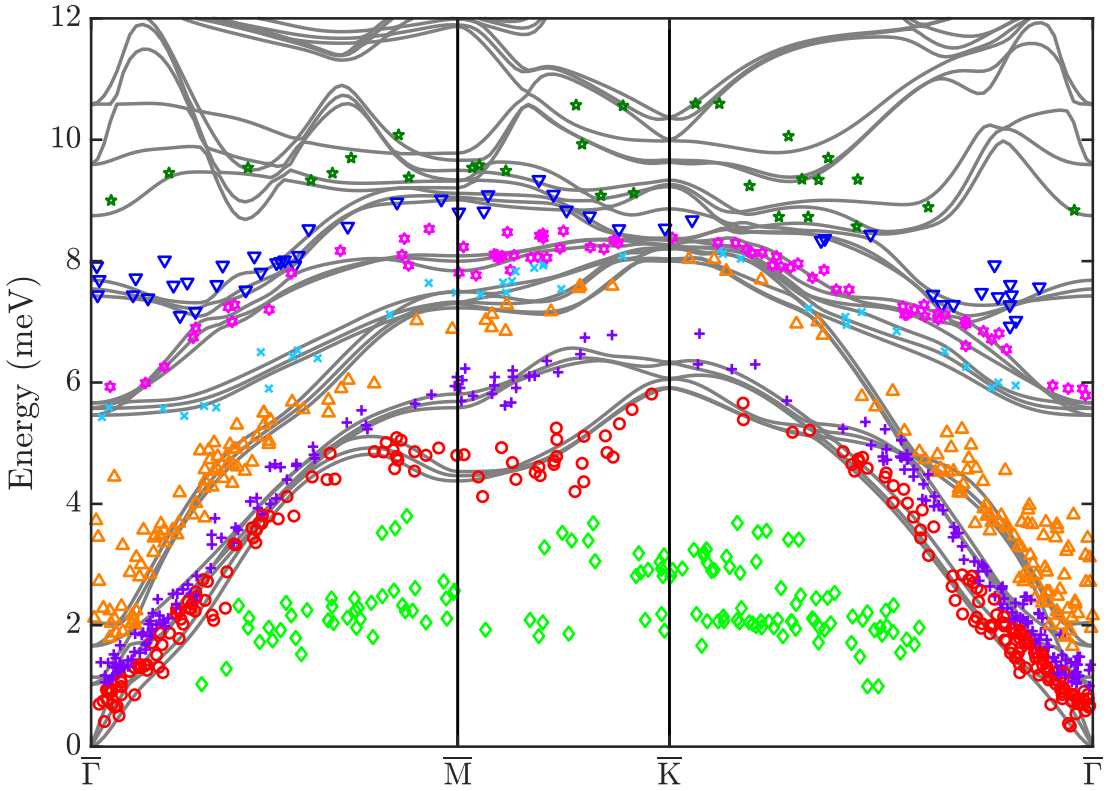


Figure 6.8: Experimental surface phonon dispersion of $Sb_2Te_3(111)$ from helium atom scattering (symbols) in comparison with DFPT calculations for three quintuple layers (solid grey lines). The assignment of the data points (colour and tag) is based on the proximity to the theoretical modes.

In figure 6.8 the final surface phonon dispersion with all phonon events, assigned to the related modes, is plotted together with the low energy events (green diamonds) and the theoretical surface phonon dispersion. In general the experimental surface phonon dispersion is in good agreement with the DFPT calculations.

## 6.5 Phonon Group Velocity

The energetically lowest mode in the surface phonon dispersion is the Rayleigh mode. Its band starts at zero energy at the $\overline{\Gamma}$-point of the surface Brillouin zone with a linear dispersion for low energies. By determining the slope of the Rayleigh mode in the linear region, the speed of surface acoustic waves, polarised in the sagittal plane, can be calculated.

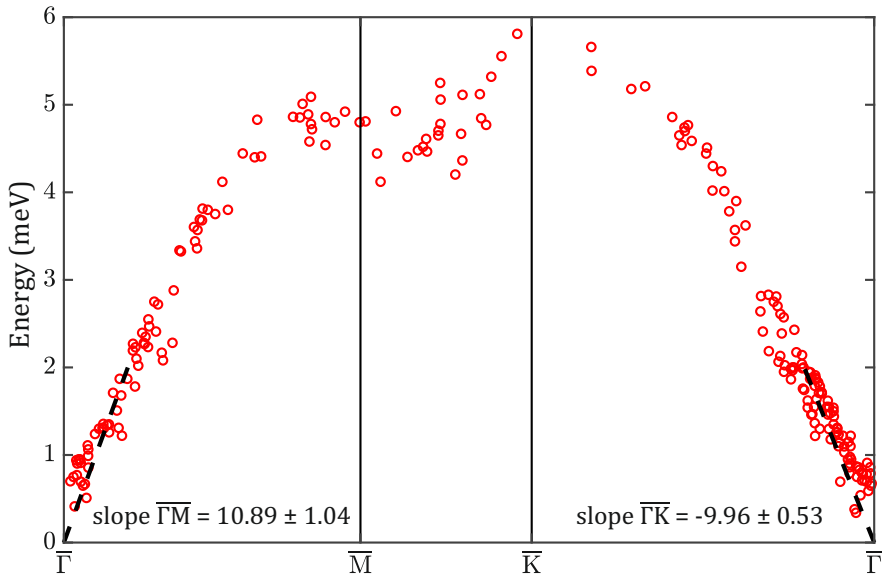


Figure 6.9: Linear fit of all measurement points from the $\overline{\Gamma}$-point origin, which have been assigned to the low energy Rayleigh mode. With the slope of the fit, the surface accoustic wave velocity can be calculated.

As illustrated in figure 6.9, surface phonon states from TOF measurement were assigned to the Rayleigh mode by comparison with $ab-initio$ calculated data by DFPT [51]. The measured points were fitted with a linear relation in the low energy range with assuming an intercept with the $\overline{\Gamma}$-point at $\Delta E = 0$. Due to the fact, that for $Sb_2Te_3$ the Rayleigh mode and the second acoustic mode proceed parallel and rather close to each other, the assignment of measured points is not always unambiguous, which leads to a rather high uncertainty for the determined slopes for $\overline{\Gamma M}$ and $\overline{\Gamma K}$ in table 6.1. From these slopes the Rayleigh group velocity can be calculated by dividing by $\hbar$.

Table 6.1: This table shows the slopes of the Rayleigh mode in $\overline{\Gamma M}$ and $\overline{\Gamma K}$ direction based on a linear fit with their corresponding group velocities.

| | slope (meV Å) | $v_R$ ($m\,s^{-1}$) |
|---|---|---|
| $\overline{\Gamma M}$ | 10.9 ± 1.0 | 1650 ± 160 |
| $\overline{\Gamma K}$ | -10.0 ± 0.5 | 1590 ± 80 |

For an elastic and isotropic material, the Rayleigh group velocity $v_R$ can be calculated in good approximation from its ratio $\zeta = \frac{v_R}{v_T}$ with the speed of sound of transverse waves $v_T$ in the bulk [54]. According to equation 6.2, the so called Poisson's ratio $\sigma$ can be calculated from the sound velocity of longitudinal $v_T$ and transverse waves $v_L$ in the bulk. The values for the acoustic velocities have been taken from literature [55], with $v_T = 1950\,m\,s^{-1}$ and $v_L = 3380\,m\,s^{-1}$.

$$\sigma = \frac{1 - 2v_T^2/v_L^2}{2(1 - v_T^2/v_L^2)} \tag{6.2}$$

$$\zeta = \frac{0.87 + 1.12\sigma}{1 + \sigma} \tag{6.3}$$

Inserting $\sigma$ into equation 6.3 returns a calculated ratio $\zeta = \frac{v_R}{v_T}$. From this the Rayleigh group velocity is determined to $v_R = 1794\ m\,s^{-1}$, which is in reasonable agreement with the group velocities gained for $\overline{\Gamma M}$ and $\overline{\Gamma K}$ in table 6.1.

## 6.6 Low Energy Modes

In figure 6.10 all data points are plotted, which appear in a low-energy region below the Rayleigh mode. Comparison with the DFPT calculations shows that these cannot be assigned to any surface phonon mode. One could possibly ascribe two separate branches with a dispersion to the plotted data points though it is difficult to do so given the number of data points and their spread.
Most low energy events keep appearing in sequential measurements for a small range of incident angles corresponding to small variations of the scan curve. This means observable low energy events are cumulated around specific incident angles. In figure 6.11 a TOF measurement series with small changes of the incident angle is shown. The annihilation part of the energy transfer spectra, with the high diffuse elastic peak on the left, provides a low energy event for several incident angles at about 3 meV.
In the following, several possible scenarios which could account for these low-energy modes are discussed.

(a) The modes provide some similarity with the recent observation of two additional dispersion curves in the energy region below the Rayleigh mode of the

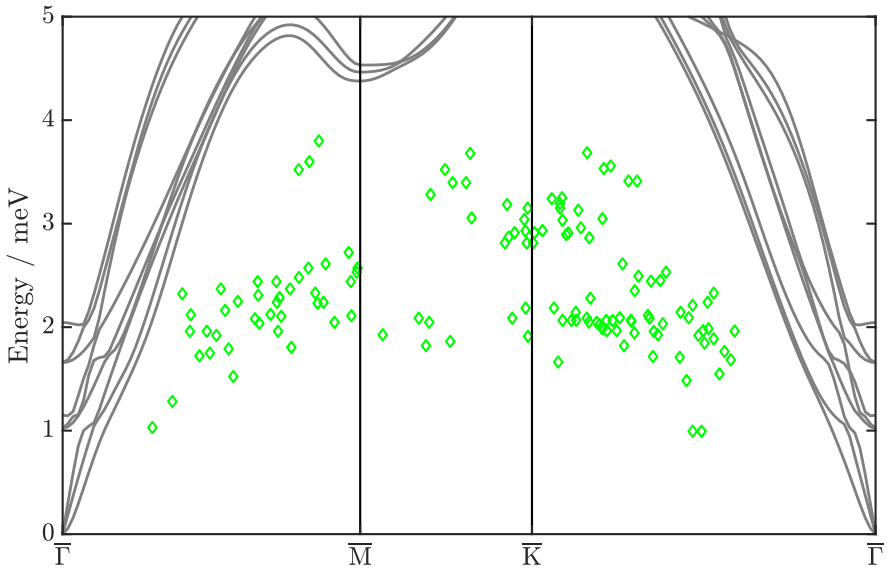


Figure 6.10: Low energy events in the region below the Rayleigh mode, which cannot be assigned to any surface phonon mode.

topological semimetal Sb(111) [56]. In the latter case the low-energy modes were assigned to elementary excitations associated to phasons and amplitons of a multi-valley charge density wave (CDW). The character of these mulitvalley CDW peaks was further confirmed by additional elastic diffraction peaks, occurring due to the presence of electron holes and pockets of the electronic structure upon crossing the Fermi level. On the one hand, the calculated electronic structure of $Sb_2Te_3$ provides also electron pocket states, occurring at about 0.2-0.3 $Å^{-1}$ along the $\overline{\Gamma M}$ azimuth. On the other hand no clear signature of additional diffraction peaks could be observed in the elastic diffraction spectra of $Sb_2Te_3$.

(b) Recent measurements of $Bi_2Se_3$ showed also additional dispersion curves in the gap below the Rayleigh mode, which were assigned to collective electronic excitations similar to surface plasmons[46]. As reported in an electron scattering study, an anomalously low acoustic surface plasmon could be observed in $Bi_2Se_3$ [57] - which would however overlap with the Rayleigh mode. The assignment of the low-energy modes in $Sb_2Te_3$(111) to similar low energy collective electronic excitations could probably be associated with a small surface charge density and an appreciable electron-phonon coupling. However, given the limited number of data points and the anomalously low energy of these modes, more detailed experiments and theoretical analysis are required in order to unambiguously assign and understand these excitations.

(c) Additional inelastic peaks may also occur in the presence of multi phonon processes. A two-phonon process yielding to an energy below the Rayleigh mode, requires a simultaneous annihilation and creation event giving rise to an energy

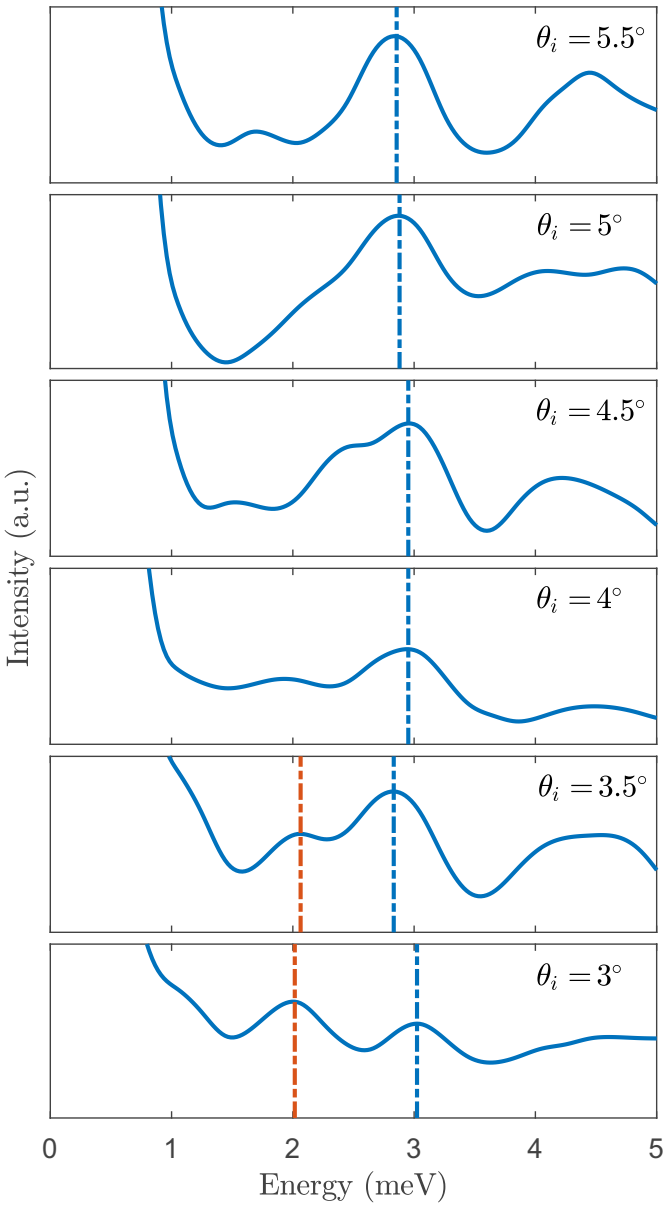


Figure 6.11: Section of the annihilation side of several energy transfer spectra, show the same low energy events at similar incident angles, decreasing in 0.5° steps. The measurements were taken in $\overline{\Gamma K}$ direction with an incident energy of 10.25 meV. The low energy events show up consistently for a small range of incident angles (dotted blue lines), while their energies stay rather constant at about 3 meV. For the bottom two measurement at 3° and 3.5° a second low energy event appears at about 2 meV (dotted orange lines).

sum below the one of a single Rayleigh mode event. In literature more or less stringent criteria for the dominance of one-phonon processes can be found. Based on the Debye-Waller factor, a criterion [18] in the high temperature regime is:

$$2W < 1 \qquad \text{for} \qquad \frac{T}{\theta_{SD}} > 0.7 \tag{6.4}$$

Measurement conditions in this work tend to be located near or slightly above this limit. Therefore multi phonon processes can not be excluded.
Independently of the above, multi phonon events show as a combination of bands in a rather uniform way. Hence an appearance in the shape of a sharp peak in the energy transfer spectrum is questionable.

(d) The low-lying vibrational modes of adsorbates are another possible source of these data points. However, frustrated translational modes of adsorbates like CO would show no dispersion and they would appear at higher vibrational energies [58].

# 7 Summary and Conclusions

In this work the surface dynamical properties of the topological insulator $Sb_2Te_3(111)$ were investigated by helium atom scattering. From elastic scattering the diffraction pattern was used to determine the surface lattice constant, yielding $a = (4.242 \pm 0.006)$ Å at room temperature and $a = (4.225 \pm 0.006)$ Å at -160 °C and thus a slightly smaller surface lattice constant, when compared to bulk measurements at similar temperatures. From the lattice constant at two different temperatures a linear thermal expansion of $\alpha = (2.2 \pm 0.8) \cdot 10^{-5}$ $K^{-1}$ is obtained. From the thermal attenuation at specular condition, the Debye-Waller factor was determined, which further allows to obtain a surface Debye-temperature of $\theta_D = (141 \pm 3)$ K, assuming an effective mass of the surface atoms equal to the atomic mass of tellurium.
Based on a new introduced method, recently published for topological insulator compounds similar to $Sb_2Te_3$, the Debye-Waller factor was used to determine the electron-phonon coupling constant with $\lambda = 0.14$, being smaller than the reported constants of the other binary topological insulators.
Inelastic scattering events were investigated in terms of time of flight measurements for various incident angles, energies and surface temperatures. Measurements were done with the sample aligned along the two high symmetry directions $\overline{\Gamma K}$ and $\overline{\Gamma M}$ of the surface Brillouin zone, respectively. The inelastic scattering spectra are mostly dominated by a high intensity of the three modes in accordance to inelastic measurements of other binary topological insulator surfaces.
Based on a data set of over 300 TOF measurements, the entire surface phonon dispersion was obtained. The experimental results were compared to theoretical calculations from density functional perturbation theory, which provide reasonably good agreement. From the slope of the Rayleigh wave the surface phonon group velocity was determined as $v_R = 1794\,\mathrm{m\,s^{-1}}$.
Based on theoretical calculations of the transverse and longitudinal acoustic velocity in the bulk, the surface phonon group velocity was approximated, which exhibits the same range of magnitude, compared to experimental results.
Noticeable are several low energy events, located below the Rayleigh mode, possibly due to collective electronic excitations, which require further investigations for an unambiguous assignment.

# Danksagung

Ich möchte an dieser Stelle die Gelegenheit nutzen um einigen Personen, die mich im Zuge dieser Arbeit oder meines Studiums begleitet haben meinen Dank auszusprechen.
Bedanken möchte ich mich bei meinem Betreuer Professor Wolfgang E. Ernst, für die Gelegenheit in der Forschungsgruppe Heliumstreuung mitzuarbeiten und Erfahrungen zu sammeln, sowie für seine Unterstützung und das entgegengebrachte Vertrauen und Verständnis.
Weiters bedanken möchte ich mich auch bei meinen Kollegen für die freundliche Aufnahme und deren Hilfsbereitschaft. Anton Tamtögl, welcher sich stets die Zeit nahm um Fragen zu diskutieren, Unklarheiten zu beseitigen und eine große Unterstützung beim Verfassen meiner Arbeit war. Adrian Ruckhofer für die tolle Einführung in die Arbeit mit der Anlage, seine Unterstützung bei den Messungen und generelle Bereitschaft bei Fragen und Problemen zu helfen.
Ganz allgemein möchte ich allen Mitarbeiten des Instituts für Experimental Physik für das kollegiale und angenehme Arbeitsumfeld danken, welches ich nicht als selbstverständlich erachte.
Dank gebührt auch jenen Studienkollegen, welche im Laufe des Studiums zu Freunden wurden, immer zu einem kleinen Plausch oder etwas Ablenkung in den Pausen zu Verfügung standen und stets um eine adäquate Kaffeeversorgung bemüht waren.
Zu guter Letzt möchte ich auch ganz besonders meinen Geschwistern und meinen Eltern für ihre Geduld, ihr Verständnis und ihre Unterstützung danken, welche mir durch das Studium geholfen hat.

# Bibliography


1. Wuttig, M. & Yamada, N. Phase-Change Materials for Rewriteable Data Storage. *Nat. Mater.* **6,** 824–832 (Nov. 2007).
2. Snyder, G. J. & Toberer, E. S. Complex Thermoelectric Materials. *Nat. Mater.* **7,** 105–114 (Feb. 2008).
3. Zhang, H., Liu, C.-X., Qi, X.-L., Dai, X., Fang, Z. & Zhang, S.-C. Topological Insulators in $Bi_2Se_3$, $Bi_2Te_3$ and $Sb_2Te_3$ with a Single Dirac Cone on the Surface. *Nat. Phys.* **5,** 438 (May 2009).
4. Pauly, C., Bihlmayer, G., Liebmann, M., Grob, M., Georgi, A., Subramaniam, D., Scholz, M. R., Sánchez-Barriga, J., Varykhalov, A., Blügel, S., Rader, O. & Morgenstern, M. Probing two Topological Surface Bands of $Sb_2Te_3$ by Spin-Polarized Photoemission Spectroscopy. *Phys. Rev. B* **86,** 235106 (Dec. 2012).
5. Seibel, C., Maaß, H., Ohtaka, M., Fiedler, S., Jünger, C., Min, C.-H., Bentmann, H., Sakamoto, K. & Reinert, F. Single Dirac Cone on the Cs-Covered Topological Insulator Surface $Sb_2Te_3(0001)$. *Phys. Rev. B* **86,** 161105 (Oct. 2012).
6. Plucinski, L., Herdt, A., Fahrendorf, S., Bihlmayer, G., Mussler, G., Döring, S., Kampmeier, J., Matthes, F., Bürgler, D. E., Grützmacher, D., Blügel, S. & Schneider, C. M. Electronic Structure, Surface Morphology and Topologically Protected Surface States of $Sb_2Te_3$ Thin Films Grown on Si(111). *J. Appl. Phys.* **113,** 053706 (Dec. 2013).
7. Reimann, J., Güdde, J., Kuroda, K., Chulkov, E. V. & Höfer, U. Spectroscopy and Dynamics of Unoccupied Electronic States of the Topological Insulators $Sb_2Te_3$ and $Sb_2Te_2S$. *Phys. Rev. B* **90,** 081106 (Aug. 2014).
8. Yavorsky, B. Y., Hinsche, N. F., Mertig, I. & Zahn, P. Electronic Structure and Transport Anisotropy of $Bi_2Te_3$ and $Sb_2Te_3$. *Phys. Rev. B* **84,** 165208 (Oct. 2011).
9. Tamtögl, A. *Surface Dynamics and Structure of Bi(111) from Helium Atom Scattering* PhD thesis (Graz University of Technology, 2012).
10. Balak, N. *Charakterisierung, Aufbau und Steuerung einer Ultrahochvakuum Atomstrahlanlage* MA thesis (Graz University of Technology, 2009).

11. Ruckhofer, A. *Surface Dynamics of the Topological Insulator $Bi_2Se_3$ from Helium Atom Scattering* MA thesis (Graz University of Technology Institute of Experimental Physics, 2017).

12. Tamtögl, A., Carter, E. A., Ward, D. J., Avidor, N., Kole, P. R., Jardine, A. P. & Allison, W. A Simple Sample Transfer Alignment for Ultra-High Vacuum Systems. *Rev. Sci. Instrum.* **87,** 066108 (Dec. 2016).

13. Pauly, H. *Atom, Molecule, and Cluster Beams I* 364 pp. (Springer Berlin Heidelberg, Dec. 1, 2010).

14. Scoles, G., Miller, D. R., Gentry, W., Pauly, H., Bassi, D., U.Hefter, Bergman, K., Zen, M., Reuss, J., Meijdenberg, C. J. N., Abuerbach, D., Kappes, M., Leutwyler, S., Valbusa, U., Buck, U., Lee, Y. T., Dagdigian, P., Stolte, S., Düren, R. & Iannotta, S. *Atomic and Molecular Beam Methods: Vol. 1* (Jan. 1998).

15. Kittel, C. *Introduction to Solid State Physics* 704 pp. (John Wiley & Sons Inc, Oct. 28, 2004).

16. Steurer, W., Apfolter, A., Koch, M., Ernst, W. E., Søndergård, E., Manson, J. R. & Holst, B. Vibrational Excitations of Glass Observed using Helium Atom Scattering. *J. Phys.: Condens. Matter* **20,** 224003 (May 2008).

17. Jardine, A. P., Alexandrowicz, G., Hedgeland, H., Allison, W. & Ellis, J. Studying the Microscopic Nature of Diffusion with Helium-3 Spin-Echo. *Phys. Chem. Chem. Phys.* **11,** 3355–3374 (18 2009).

18. Benedek, G. & Toennies, J. P. *Atomic Scale Dynamics at Surfaces* (Springer Berlin Heidelberg, Dec. 28, 2018).

19. Farias, D. & Rieder, K.-H. Atomic Beam Diffraction from Solid Surfaces. *Rep. Prog. Phys.* **61,** 1575–1664 (Dec. 1998).

20. Manson, J. R., Benedek, G. & Miret-Artés, S. Electron-Phonon Coupling Strength at Metal Surfaces Directly Determined from the Helium Atom Scattering Debye-Waller Factor. *J. Phys. Chem. Lett.* **7,** 1016–1021 (Mar. 2016).

21. Tamtögl, A., Kraus, P., Avidor, N., Bremholm, M., Hedegaard, E. M. J., Iversen, B. B., Bianchi, M., Hofmann, P., Ellis, J., Allison, W., Benedek, G. & Ernst, W. E. Electron-Phonon Coupling and Surface Debye Temperature of $Bi_2Te_3$(111) from Helium Atom Scattering. *Phys. Rev. B* **95,** 195401 (May 2017).

22. Toennies, J. P. in *Surface Phonons* (eds Kress, W. & de Wette, F. W.) 111–166 (Springer Berlin Heidelberg, Berlin, Heidelberg, 1991).

23. Mayrhofer-Reinhartshuber, M. *Helium Atom Scattering from Surfaces including the Pseudo Random Chopper Technique* MA thesis (Institute of Experimental Physics, 2010).

24. Pauly, H. *Atom, Molecule, and Cluster Beams II* 396 pp. (Springer Berlin Heidelberg, Dec. 4, 2010).

25. Benedek, G., Brusdeylins, G., Bruce Doak, R., Skofronick, J. G. & Toennies, J. P. Measurement of the Rayleigh Surface-Phonon Dispersion Curve for NaCl(001) from High-Resolution He Time of Flight Spectroscopy and from Kinematical Focusing Angles. *Phys. Rev. B* **28,** 2104–2113 (Aug. 1983).

26. Hicks, L. D. & Dresselhaus, M. S. Use of Quantum-Well Superlattices to Obtain a High Figure of Merit from Nonconventional Thermoelectric Materials. *MRS Proc.* **326,** 413 (1993).

27. Zastrow, S., Gooth, J., Boehnert, T., Heiderich, S., Toellner, W., Heimann, S., Schulz, S. & Nielsch, K. Thermoelectric Transport and Hall Measurements of Low Defect $Sb_2Te_3$ Thin Films grown by Atomic Layer Deposition. *Semicond. Sci. Technol.* **28,** 035010 (Feb. 2013).

28. Zhang, Z., Zhang, H., Wu, Y., Zeng, Z. & Hu, Z. Optimization of the Thermopower of Antimony Telluride Thin Film by Introducing Tellurium Nanoparticles. *Appl. Phys. A* **118,** 1043–1051 (Mar. 2015).

29. Hinsche, N. F., Zastrow, S., Gooth, J., Pudewill, L., Zierold, R., Rittweger, F., Rauch, T., Henk, J., Nielsch, K. & Mertig, I. Impact of the Topological Surface State on the Thermoelectric Transport in $Sb_2Te_3$ Thin Films. *ACS Nano* **9,** 4406–4411 (Apr. 2015).

30. Fujimori, S., Yagi, S., Yamazaki, H. & Funakoshi, N. Crystallization Process of Sb-Te Alloy Films for Optical Storage. *J. Appl. Phys.* **64,** 1000–1004. eprint: `https://doi.org/10.1063/1.341908` (1988).

31. Zhang, J., Chang, C.-Z., Zhang, Z., Wen, J., Feng, X., Li, K., Liu, M., He, K., Wang, L., Chen, X., Xue, Q.-K., Ma, X. & Wang, Y. Band Structure Engineering in $(Bi_{1-x}Sb_x)_2Te_3$ Ternary Topological Insulators. *Nat. Commun.* **2,** 574 (Dec. 2011).

32. Sessi, P., Storz, O., Bathon, T., Wilfert, S., Kokh, K. A., Tereshchenko, O. E., Bihlmayer, G. & Bode, M. Scattering Properties of the Three-Dimensional Topological Insulator $Sb_2Te_3$: Coexistence of Topologically Trivial and Nontrivial Surface States with Opposite Spin-Momentum Helicity. *Phys. Rev. B* **93,** 035110 (Jan. 2016).

33. Novoselov, K. S., Geim, A. K., Morozov, S. V., Jiang, D., Katsnelson, M. I., Grigorieva, I. V., Dubonos, S. V. & Firsov, A. A. Two-Dimensional Gas of Massless Dirac Fermions in Graphene. *Nature* **438,** 197–200 (Nov. 2005).

34. Wu, C., Bernevig, B. A. & Zhang, S.-C. Helical Liquid and the Edge of Quantum Spin Hall Systems. *Phys. Rev. Lett.* **96,** 106401 (Mar. 2006).

35. Qi, X.-L. & Zhang, S.-C. The Quantum Spin Hall Effect and Topological Insulators. *Phys. Today* **63,** 33–38 (Jan. 2010).

36. Zhu, S., Ishida, Y., Kuroda, K., Sumida, K., Ye, M., Wang, J., Pan, H., Taniguchi, M., Qiao, S., Shin, S. & Kimura, A. Ultrafast Electron Dynamics at the Dirac Node of the Topological Insulator $Sb_2Te_3$. *Sci. Rep.* **5,** 13213 (Aug. 2015).

37. Wang, G., Zhu, X., Wen, J., Chen, X., He, K., Wang, L., Ma, X., Liu, Y., Dai, X., Fang, Z., Jia, J. & Xue, Q. Atomically Smooth Ultrathin Films of Topological Insulator $Sb_2Te_3$. *Nano Res.* **3,** 874–880 (Dec. 2010).

38. Davis, L. E. *Handbook of Auger Electron Spectroscopy: A Reference Book of Standard Data for Identification and Interpretation of Auger Electron Spectroscopy Data* (Physical Electronics, 1996).

39. Chen, X., Zhou, H. D., Kiswandhi, A., Miotkowski, I., Chen, Y. P., Sharma, P. A., Lima Sharma, A. L., Hekmaty, M. A., Smirnov, D. & Jiang, Z. Thermal Expansion Coefficients of $Bi_2Se_3$ and $Sb_2Te_3$ Crystals from 10 K to 270 K. *Appl. Phys. Lett.* **99,** 261912 (Jan. 2011).

40. Bessas, D., Sergueev, I., Wille, H.-C., Perßon, J., Ebling, D. & Hermann, R. P. Lattice Dynamics in $Bi_2Te_3$ and $Sb_2Te_3$: Te and Sb Density of Phonon States. *Phys. Rev. B* **86,** 224301 (Dec. 2012).

41. Anderson, T. L. & Krause, H. B. Refinement of the $Sb_2Te_3$ and $Sb_2Te_2Se$ Structures and Their Relationship to Nonstoichiometric $Sb_2Te_{3-y}Se_y$ Compounds. *Acta Crystallogr., Sect. B* **30,** 1307–1310 (May 1974).

42. Semiletov, S. The Electron Diffraction Analysis of the Structure of Antimony Telluride. *Kristallografiya* **1,** 403–406 (1956).

43. Ruckhofer, A., Tamtögl, A., Pusterhofer, M., Bremholm, M. & Ernst, W. E. Helium-Surface Interaction and Electronic Corrugation of Bi2Se3(111). *J. Phys. Chem. C* **123,** 17829–17841 (July 2019).

44. *Non-Tetrahedrally Bonded Elements and Binary Compounds I: Supplement to Vols. III/17e, f (Print Version) Revised and Updated Edition of Vols. III/17e, ... - New Series) (Volumes III/17e Vol 41)* (Springer, 1998).

45. Benedek, G., Miret-Artés, S., Toennies, J. P. & Manson, J. R. Electron-Phonon Coupling Constant of Metallic Overlayers from Specular He Atom Scattering. *J. Phys. Chem. Lett.* **9,** 76–83 (Jan. 2018).

46. Ruckhofer, A., Campi, D., Bremholm, M., Hofmann, P., Bendek, G., Bernasconi, M., Ernst, W. E. & Tamtögl, A. THz Surface Modes and Electron-Phonon Coupling in $Bi_2Se_3$(111). *arXiv e-prints,* arXiv:1907.01864. arXiv: `1907.01864 [cond-mat.mtrl-sci]` (July 2019).

47. Anemone, G., Taleb, A. A., Benedek, G., Castellanos-Gomez, A. & Farías, D. Electron-Phonon Coupling Constant of 2H-MoS2(0001) from Helium-Atom Scattering. *J. Phys. Chem. C* **123,** 3682–3686 (Feb. 2019).

48. Jariwala, B. S., Shah, D. V., Vyas, S. M. & Pandya, G. R. Ac and Dielectric Behavior of $Sb_2Te_3$ Single Crystal. *AIP Conf. Proc.* **1349,** 1107–1108 (Feb. 2011).

49. Yin, J., Krishnamoorthy, H. N. S., Adamo, G., Dubrovkin, A. M., Chong, Y., Zheludev, N. I. & Soci, C. Plasmonics of Topological Insulators at Optical Frequencies. *NPG Asia Mater.* **9,** e425–e425 (Aug. 2017).

50. Benedek, G., Miret-Artés, S., Manson, J. R., Ruckhofer, A., Ernst, W. E. & Tamtögl, A. Origin of the Electron-Phonon Interaction of Topological Semimetal Surfaces Measured with Helium Atom Scattering. *J. Phys. Chem. Lett.* 1927–1933 (Feb. 2020).

51. Campi, D., Bernasconi, M. & Benedek, G. Ab-initio Calculation of Surface Phonons at the $Sb_2Te_3$(111) Surface. *Surf. Sci.* **678.** Surface Structure and Dynamics – in Honor of Karl-Heinz Rieder, 46–51 (2018).

52. Allison, W., Willis, R. F. & Cardillo, M. Origin of the Anomalous Low-Frequency Losses observed in the Inelastic Scattering of He Atoms from LiF(001). *Phys. Rev. B* **23,** 6824–6827 (12 June 1981).

53. Richter, W. & Becker, C. R. A Raman and Far-Infrared Investigation of Phonons in the Rhombohedral $V_2$-$VI_3$ Compounds $Bi_2Te_3$, $Bi_2Se_3$, $Sb_2Te_3$ and $Bi_2(Te_{1-x}Se_x)_3$ $(0 < x < 1)$, $(Bi_{1-y}Sb_y)_2Te_3$ $(0 < y < 1)$. *Phys. Status Solidi B* **84,** 619–628 (Mar. 1977).

54. Kress, W. & Wette, F. W. d. ( *Surface Phonons* (Springer, 1991).

55. Lu, Q., Zhang, H.-Y., Cheng, Y., Chen, X.-R. & Ji, G.-F. Phase Transition, Elastic and Electronic Properties of Topological Insulator $Sb_2Te_3$ under Pressure: First Principle Study. *Chinese Physics B* **25,** 026401 (Feb. 2016).

56. Tamtögl, A., Kraus, P., Mayrhofer-Reinhartshuber, M., Benedek, G., Bernasconi, M., Dragoni, D., Campi, D. & Ernst, W. E. Statics and Dynamics of Multivalley Charge Density Waves in Sb(111). *npj Quantum Mater.* **4,** 28 (June 2019).

57. Jia, X., Zhang, S., Sankar, R., Chou, F.-C., Wang, W., Kempa, K., Plummer, E. W., Zhang, J., Zhu, X. & Guo, J. Anomalous Acoustic Plasmon Mode from Topologically Protected States. *Phys. Rev. Lett.* **119,** 136805 (Sept. 2017).

58. Graham, A. P. The Low Energy Dynamics of Adsorbates on Metal Surfaces Investigated with Helium Atom Scattering. *Surf. Sci. Rep.* **49,** 115–168 (Apr. 2003).